university of groningen

medusa

Radon corrections in geophysical surveys with a split γ-ray detector

Master thesis physics

Student: M.K. Mijland, s3099474

Daily supervisor: dr. Steven van der Veeke

First examiner: prof. dr. ir. Ronnie Hoekstra

Second examiner: dr. Emiel van der Graaf

Date: June 5, 2023

Abstract

This thesis presents a research project conducted at Medusa Radiometrics, a company producing specialised γ-spectrometers for geophysics. These spectrometers are used as survey tools to determine concentrations of naturally occurring radionuclides, including ^{40}K, ^{232}Th, and ^{238}U, in soil. The concentrations of these radionuclides serve as predictors of other soil qualities, such as sediment texture, nutrient content and more. The presence of ^{222}Rn, a radioactive noble gas originating from the decay chain of ^{238}U, in the atmosphere can lead to erroneous measurements of elevated ^{238}U concentrations in the soil due to the similar γ-ray emissions. This research focused on developing a novel method using a split γ-ray detector with directional sensitivity to distinguish atmospheric ^{222}Rn from ^{238}U in the ground. The directional dependence was characterized by assessing the detector's response at various angles, approximating the change with a cosine function, which turned out to be a good approximation. The method's effectiveness was evaluated by comparing its ^{222}Rn and ^{238}U measurements with those from the Lutjewad atmospheric measurement station. The results showed that the ^{238}U concentration determined by this method was nearly independent of atmospheric ^{222}Rn concentration. Although the measured ^{222}Rn concentration was higher than that of Lutjewad, the two concentrations were correlated with a correlation coefficient of $r = 0.64$, data smoothing was able to improve this to $r = 0.88$.

Contents

Chapter 1

Introduction

1.1 Medusa Radiometrics

This thesis documents a research project conducted on behalf of Medusa Radiometrics, a leading company specializing in the manufacturing of γ-ray spectrometers and complementary analysis software. Medusa originated as a spin-off from the nuclear physics lab of the University of Groningen. These tools find wide-ranging applications in diverse fields such as mining, agriculture, soil mapping, nuclear research, and radiation safety [1].

1.2 Geophysical γ-ray surveys

Gamma-ray spectrometers are extensively utilized in geophysics to map the concentrations of naturally occurring radionuclides, specifically ^{40}K, ^{238}U, and ^{232}Th, in the environment [2]. The radionuclide concentrations serve as proxies for sediment composition [3][4][5], non-radioactive contamination [6][7], and soil texture [8][9]. These applications enable studies in mineral exploration [10][2], precision agriculture, and the distribution of non-radioactive contaminants in the environment.

The continuous decay of naturally present radionuclides in the ground emits a steady flux of γ radiation, which is captured and analysed by spectrometers during geophysical surveys. Such surveys involve moving the spectrometer across the area of interest to record the radiation [2]. This non-intrusive approach allows for the assessment of spatial variations in radionuclide distribution.

Gamma-ray surveys can be conducted from various platforms, including airborne, UAV-borne (unmanned aerial vehicle), ground-based, and underwater. Airborne surveys employ spectrometers mounted on small aircraft or helicopters, offering broad coverage but lower spatial resolution. UAV-borne surveys, similar to airborne surveys, involve the use of UAVs as platforms for conducting γ-ray surveys. In UAV-borne surveys, the UAV flies at lower altitudes and is equipped with smaller detectors compared to traditional airborne

surveys. Ground-based surveys involve walking or driving with the spectrometer, capturing smaller areas with higher spatial resolution. Underwater surveys employ water-tight housings for spectrometers, which are dragged along the bottom of seas, lakes, or rivers. Each implementation has its own scale and resolution, with airborne surveys covering larger areas at a relatively lower spatial resolution and ground-based surveys providing finer details within smaller areas. The utilization of UAV-borne platforms bridges the gap between ground-based and airborne platforms, offering an intermediate level of spatial resolution and survey coverage [11].

1.3 Radon presence in geophysical surveys

Radon, specifically ^{222}Rn, is a noble gas that originates in the ground as part of the ^{238}U decay chain. With a half-life of 3.81 days [12] and chemical inertness, it can escape from the ground into the atmosphere where it undergoes radioactive decay. The emitted γ-rays from ^{222}Rn and its decay products exhibit similar characteristics to those of ^{238}U. Consequently, the presence of atmospheric ^{222}Rn can lead to erroneous measurements of elevated ^{238}U concentrations.

Many methods exist for correcting the presence of ^{222}Rn during geophysical surveys, with most of them being designed for airborne geophysical surveys. In the work of S. van der Veeke [11], two new radon-correction methods are proposed specifically for UAV-borne geophysical surveys. One of these methods involves the use of a split γ-ray spectrometer, made with a scintillation crystal that is split into two halves. One half faces the sky while the other faces the ground. Leveraging its directional sensitivity, this detector can potentially distinguish between radiation originating from atmospheric ^{222}Rn and ^{238}U in the ground.

1.4 Aim and Content of the thesis

A prototype of the split γ-ray spectrometer was constructed by Medusa Radiometrics. The purpose of this research is to assess and characterize the performance of this detector and evaluate its suitability as a method for radon correction in geophysical surveys.

The main research question of this thesis is: Can the split detector be used to correct for the presence of ^{222}Rn during geophysical surveys?

1. How should the split detector be calibrated, such that it is capable of measuring the concentrations of ^{222}Rn, ^{238}U and other radionuclides?
2. What is the effect of rotations on the output of the split detector?

3. Is the split detector capable of determining the atmospheric ^{222}Rn concentration?

4. Does the corrected ^{238}U signal depend on the atmospheric ^{222}Rn concentration?

In Chapter 2, a brief explanation of the theoretical background related to radioactive decay, naturally occurring radiation, γ-ray detection, and spectrum analysis is provided, along with an overview of the simulation technique used in this research. Chapter 3 focuses on the influence of ^{222}Rn on γ-ray surveys, the methods used to correct for its presence, and the underlying theory behind these methods. The design and calibration procedure of the split γ-ray detector, along with a brief investigation of the calibration setup at Medusa Radiometrics, are detailed in Chapter 4. Chapter 5 explores the directional sensitivity of the detector by studying its response when oriented at various angles. In Chapter 6, the effectiveness of the split detector in filtering out ^{222}Rn signal is examined through a stationary measurement, comparing the ^{222}Rn and ^{238}U measurements with the split detector with an independent ^{222}Rn measurement. Finally, Chapter 7 summarizes the key findings of the research.

Chapter 2

Background information

2.1 Introduction

This chapter intends to acquaint the reader with the physics and technology relevant to γ-ray spectrometry and geophysical surveys in the context of this research. The fundamentals of radioactive decay are explained in Section 2.2. Section 2.3 elucidates the naturally occurring radionuclides that are pertinent to γ-ray spectrometry and their decay processes. The interaction between γ-radiation and matter is expounded in Section 2.4, followed by Section 2.5, which delves into the detection of γ-rays, particularly by the detectors employed in geophysics. Subsequently, Section 2.6 outlines the analysis of γ-ray spectra. Lastly, Section 2.7 provides a concise explanation of the Monte Carlo simulations conducted for this research.

2.2 Radioactive decay

All matter is made out of atoms, consisting of electrons and a nucleus. The nucleus consists of protons and neutrons. The number of protons (Z) determines the chemical properties of an atom, and its position on the periodic table. The number of neutrons(N) does not influence the chemical properties of an atom, but it does affect the mass. A nuclide is an atom that can be specified by its chemical and its mass number (the number of protons plus the number of neutrons $A = Z + N$). An example would be ^{238}U where U indicates the element Uranium (Z=92) and 238 the mass number.

Nuclides can be either stable or unstable, depending on the specific combination of neutrons and protons. Unstable nuclides are called radionuclides and can spontaneously decay into a different (radio)nuclide and emit radiation. The original radionuclide is called the parent and the decay product the daughter. If the daughter nuclide is still unstable, it will decay again, this will go on until a stable configuration of protons and neutrons is reached. This is called a decay chain.

The three main types of decay that occur are α-, β-, or γ-decay. In α-decay, a parent-nucleus is split into 2 parts, one daughter nucleus and one α-particle which is a ^{4}He nucleus. β-decay occurs in either β^- or β^+ decay, in which the parent nucleus emits an electron or positron (so called β-rays), respectively. The daughter nucleus will have the number of protons Z go up by one in case of β^- and down in case of β^+. The atomic mass number A stays the same in β-decay. In γ-decay, high energy photons are emitted. After an α- or β-decay, the daughter nucleus is often left in an excited state. The daughter nucleus then decays to a lower excited state or its ground state, during this a highly energetic photon (γ-ray) is emitted with an energy equal to the energy difference between the states.

The probability that a radionuclide will decay is constant in time. It is not possible to say when a single decay will happen, but on average the number of radionuclides at a certain time can be predicted. This can be done using the half-life ($T_{1/2}$) of a radionuclide, the time it takes on average for half of the radionuclides to decay. The half-life is a measure for the instability of a radionuclide, a shorter half-life means a more unstable nucleus. Starting with N_0 radionuclides, the total number $N(t)$ over time (t) is given by:

$$N(t) = N_0 e^{-\lambda t} \tag{2.1}$$

Where $\lambda = \frac{\ln(2)}{T_{1/2}}$ is the decay constant of the radionuclide. It is clear from equation 2.1 that the number of radionuclides decreases exponentially over time. The number of atoms that decay per unit time is called the activity(A) not to be confused with the mass number. It has the unit Becquerel (Bq) which is defined as one decay per second: 1 Bq = 1/s. The activity of a radionuclide is given by:

$$A = -\frac{dN}{dt} = \lambda N \tag{2.2}$$

The activity will also exponentially decrease over time if no atoms are added, because it is proportional to the number of radioactive atoms. In the case of a series of decays, where the parent nuclide has a half-life that is much longer than that of its daughters, the activity of the daughters will eventually become equal to that of the parent. This situation is called secular equilibrium, and it occurs assuming that no nuclides are removed from the sample through other mechanisms than decay. The rule of thumb is that it takes approximately 5 times the half-live of the daughter nucleus before the activities of parent and daughter are equal (after five half life the daughter activity is about 97 % of the parent activity), which means secular equilibrium is reached.

2.3 Radioactivity in nature

Radionuclides encountered in nature are of three origins: radionuclides that were present during the formation of the earth, radionuclides that have come into the environment due

to the efforts of humans and radionuclides produced by cosmic radiation[2].

Some radionuclides have been around since the formation of the earth, these are referred to as primordial radionuclides. The reason they are still around after billions of years is that their half-life is of the same order of magnitude. The most relevant primordial radionuclides for γ-ray spectroscopy are ^{40}K with $T_{1/2} = 1.248 \times 10^9$ years and the decay chains of ^{232}Th with $T_{1/2} = 14.0 \times 10^9$ years and ^{238}U with $T_{1/2} = 4.463 \times 10^9$ years [13]. The reason for this is that these elements are relatively plentiful in the natural surroundings, and that they are γ-emitters or products in the decay chains are γ-emitters, typical abundances on the earths crust of these elements range from 2-2.5 % K, 2-3 ppm U and 8-12 ppm Th [2].

When ^{40}K decays, there is a 10.72 % chance that it decays via electron capture to ^{40}Ar and an 89.28 % chance that it decays via β^--decay to ^{40}Ca. Both of which are stable[13]. In the case that it decays to argon, it will emit a γ-ray with an energy of 1.461 MeV[12]. This is shown in Figure 2.1. It also shows a γ-ray spectrum of a pure ^{40}K source, which is a histogram of the number of γ-rays counted by a detector per energy bin. The spectrum has a peak around 1.46 MeV, the energy of the γ-ray from the decay. The features of a γ-ray spectrum will be explained in more detail in section 2.5.1.

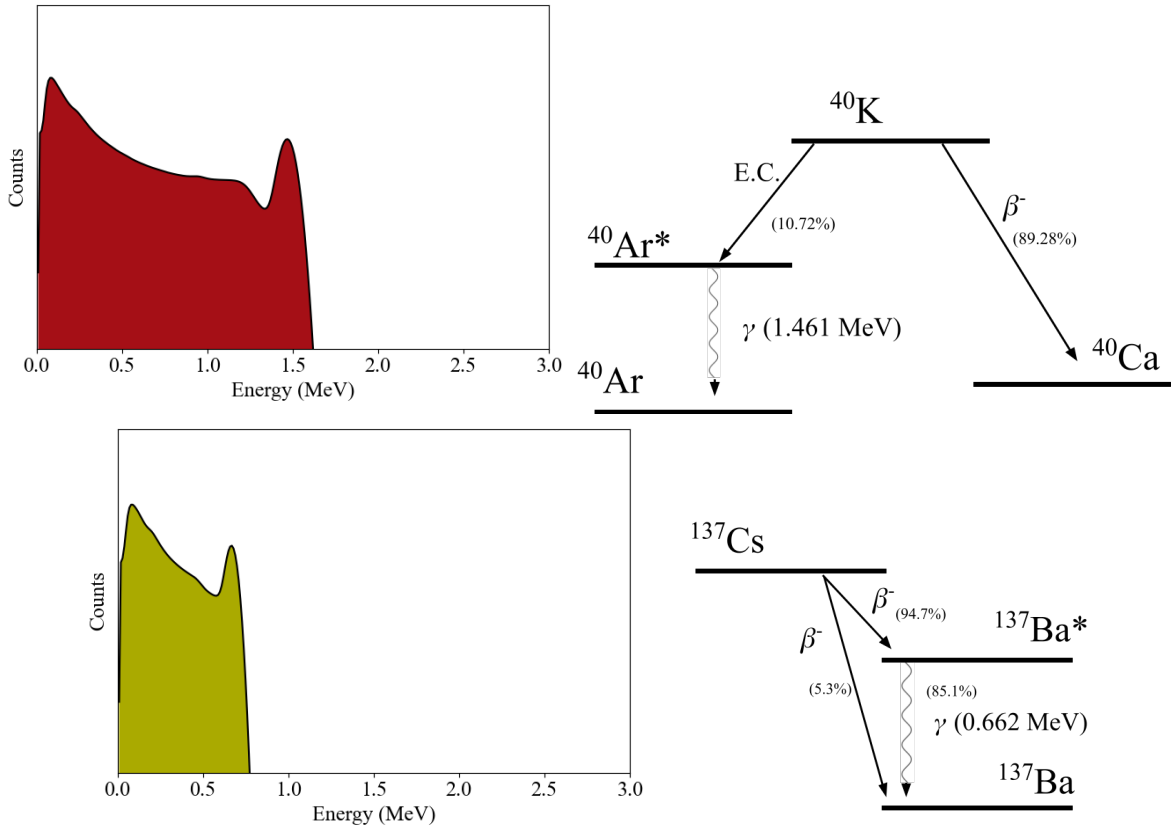

Figure 2.1: The decay schemes and γ-spectra of ^{40}K (Top) and ^{137}Cs (Bottom). The γ-spectra were created with Monte Carlo simulations of the split detector surrounded by bricks containing ^{40}K or ^{137}Cs (see 4.3).

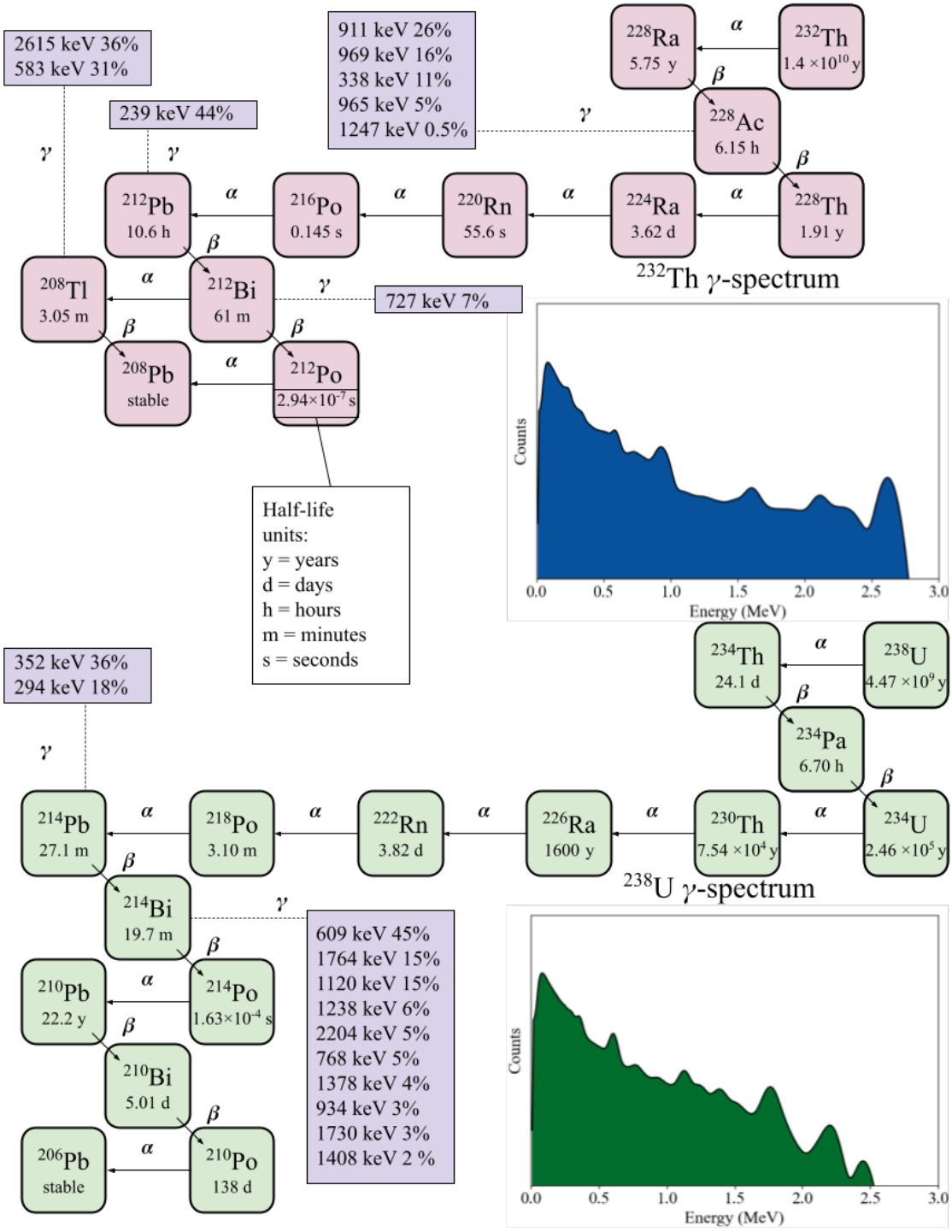

Figure 2.2: The decay-chains and γ-ray spectra of ^{232}Th (top) and ^{238}U (bottom) with the most abundant γ-ray energies of the decay chains followed by a percentage which indicates how often that γ-ray is emitted per decay of ^{232}Th or ^{238}U. The γ-spectra were created with Monte Carlo simulations of the split detector surrounded by bricks containing ^{232}Th or ^{238}U (see 4.3).

^{232}Th and ^{238}U decay via a decay chain to the stable isotopes of lead ^{208}Pb and ^{206}Pb, respectively. ^{232}Th and ^{238}U do not emit any γ-rays, but some decay products in their decay chains do. Because γ-rays of more than one energy are emitted, the γ-ray spectra of ^{232}Th and ^{238}U, shown in Figure 2.2, have multiple peaks. These spectra of ^{232}Th and ^{238}U have the underlying assumption that all radionuclides in the chain are in secular equilibrium. In nature, thorium rarely occurs out of equilibrium. Uranium is more commonly found out of equilibrium in nature, this happens because some daughters in the decay chain of ^{238}U can be selectively removed from the decay chain [2]. This can lead to an error in the measured uranium concentration, because it is estimated based on the γ-rays emitted by ^{214}Pb and ^{214}Bi, which are far down the decay chain and not necessarily in equilibrium with ^{238}U.

Radionuclides produced by humans are called anthropogenic radionuclides. The most important reasons they appear in nature are the fallout of nuclear bomb tests, and accidents in the nuclear power industry [2]. The most common anthropogenic radionuclide emitting γ-rays in nature is caesium-137 (^{137}Cs), with a half-life of 30.04 y [13]. ^{137}Cs decays via β^- decay to ^{137}Ba, which is accompanied by a γ-ray of 0.661 MeV 85.1 % of the time[12](see Figure 2.1).

Radionuclides formed in the atmosphere as a result of nuclear reactions caused by cosmic radiation are called cosmogenic radionuclides. However, they either do not emit any γ-radiation or only appear in small quantities and are not an important source of γ-radiation in geophysical surveys[11].

2.4 The interactions of γ-rays with matter

γ-rays, unlike α- and β-rays, are electrically neutral and, do not continuously lose energy as they pass through matter. Rather, they can travel a certain distance before interacting with an atom. The penetration distance of a photon is determined by the probability of interaction per unit distance travelled, which is dependent on the particular medium and the energy of the photon. This probability is called the linear attenuation coefficient (μ). The attenuation per unit mass is called the mass attenuation (μ/ρ) and is simply the linear attenuation coefficient divided by the density of the material (ρ). The number of photons that has not interacted as a function of distance travelled (x)is given by:

$$N = N_0 e^{-\mu x} \tag{2.3}$$

Upon interaction, a photon may either be absorbed or it may experience scattering, causing a change in its direction of travel, possibly losing energy in the process. The main ways in which γ-rays deposit energy into a material are the photo-electric effect, Compton scattering and pair-production.

In the photo-electric effect, the energy of a γ-ray is completely absorbed by an electron in an atom. The electron is emitted from the atom with a kinetic energy equal to that of the γ-ray minus the binding energy to the atom. This effect is the most common way for γ-rays with low energy (less than a few hundred keV) to interact, and the effect is enhanced if the medium has high atomic number Z [14].

Compton scattering is the process in which a γ-ray scatters off an electron in such a way, that some of its energy is transferred to the electron. The amount of energy given to the electron is dependent on the angle at which the γ-ray scatters off the electron. This process happens over the entire range of the γ-spectrum, but for γ-rays with an energy between a few hundred keV and several MeV, this is the most prevalent interaction. The exact energy range for which Compton scattering is the most dominant mode of interaction between γ-ray and matter is material dependent, but most of the γ-rays encountered in geophysics fall within this range for most materials. There is not a large difference in the specific mass-attenuation due to the Compton effect in different materials [15], which means the linear attenuation of the Compton effect is mostly determined by the density of a material.

Pair-production is the process wherein a photon has an interaction with an atom that produces an electron and a positron. This effect can only happen when a γ-ray has an energy of more than 1.022 MeV, the rest-mass of the electron-positron pair. The positron will inevitably find an electron at some point and annihilate, producing 2 γ-rays with an energy of 0.511 MeV, travelling in opposite directions. This effect starts occurring at 1.022 MeV, and it becomes more prominent the higher the energy of the γ-ray, for very high energies it is the dominant way for a photon to interact[15].

2.5 γ-ray detectors

γ-rays can be detected by various detectors, such as gas-filled detectors, semiconductors, organic scintillation detectors and inorganic scintillation detectors. Gas-filled detectors such as ionization chambers and Geiger-Mueller counters do not provide enough information on the energy of the incoming γ-rays to identify radionuclides. Semiconductors have a moderate Z-value and density and come with excellent energy resolution, but are limited in their applicability for in-situ measurements because of other factors. For example, High Purity Germanium (HPGe) detectors are to be cooled to below 77 K. Other semiconductors such as Cadmium Zinc Telluride (CdZnTe) detectors are limited in their size (max: 4x4x1.5 cm), which limits the detection efficiency of the detector [11]. Organic scintillation detectors (such as plastic scintillators) are made from materials with a low Z-value and a density, which causes their spectra to have less structure when measuring natural radioactivity [16].

Inorganic scintillation detectors such as NaI (Sodium Iodine), CsI (Caesium Iodine) and

BGO (Bismuth Germanate or $Bi_4Ge_3O_{12}$) are crystals with high Z-values and moderate to high densities. They are useable at room temperature, and crystals can be made in large enough sizes to measure natural radiation with the desired efficiency [16].

When ionising radiation interacts with a scintillator, it causes an electronic transition into an excited state. Electrons in the excited state will decay by emitting photons, which can then be observed. In inorganic scintillators, the energy states are determined by the crystal lattice of the material. In insulators and semiconductors, electrons can only be in discrete bands of energy, the lower energy band is the valence band in which electrons are bound in place and in the higher energy band, the conduction band electrons have enough energy to freely move around. Pure scintillation crystals are insulators, for which there is a large energy gap between the valence band and conduction band. This gap is so large for pure crystals that electrons transitioning from the conduction band to the valence band typically emit a photon outside the visible spectrum. By introducing impurities into a crystal, energy states in between the valence band and conduction band become allowed. Electrons in the conduction band can now decay to the valence band via these intermediate energy states. The energy gap for the electronic transitions is now smaller, and electrons that de-excite will emit photons of a visible wavelength [14].

Scintillators ideally have a high Z-value, density and size in order to absorb a large amount of γ-rays. The scintillator should be transparent to its own emitted radiation. The response of the scintillator should be linear with the amount of energy deposited for a large range of energies, the decay time of the excited states should be as short as possible for fast signal pulses. Finally, the refractive index of the scintillator should match that of the photomultiplier or light sensor next to it for optimal photon detection [14].

Out of the inorganic scintillators, NaI crystals have the best energy resolution, but the disadvantage of being brittle and hygroscopic, makes them less suitable for field measurements. BGO has a very high density ($\rho = 7.13\text{g/cm}^3$) and Z-value ($Z(\text{Bi}) = 83$), which makes it have the largest probability per unit volume for photoelectric absorption of any commercially available scintillation material. The light yield is relatively low, only 10-20 % of that of NaI [14]. CsI has an energy resolution that is typically slightly worse than NaI, but it makes up for that by being less hygroscopic and more durable [14]. Furthermore, it has a higher density than NaI and caesium has a higher Z-value than sodium, which increases the amount of photoelectric absorption of the crystal. For these reasons, CsI is the detector material of choice for most of the Medusa Radiometrics γ-ray spectrometers.

Reflective material is put around the scintillator crystal to trap as many photons as possible. The light from the scintillator is picked up by a photomultiplier tube or silicon photomultiplier, which turn the light into an electrical signal. A device called a multichannel analyser (MCA) is then used to create a raw MCA histogram of the received γ-radiation. By calibrating the MCA, this raw histogram can be turned into an energy

spectrum.

2.5.1 The shape of γ-ray spectra

γ-rays that lose all their energy in the detector will show up as a peak in the spectrum around the full energy of the γ-rays, this peak is called the photo-peak or full energy peak. The width of the peaks depends on the resolution of the detector. The width of the peak is measured by the Full Width at Half Maximum(FWHM), which has the unit of energy. The resolution is given as the percentage of the width with respect to the energy of the peak, Resolution $= \frac{\text{FWHM}}{\text{Peak energy}}$. Some γ-rays will lose some of their energy to Compton scattering in the detector and then manage to escape. This is the Compton continuum in the spectrum, which is the smooth part that fills the space between the peaks and becomes more prominent at low energies. In the scenario that photons undergo pair-production, the positron that is produced will meet an electron and annihilate. This produces two 0.511 MeV photons, one or both of which can escape the detector. This can be seen in the spectrum as peaks 0.511 MeV and 1.022 MeV removed from the full energy peak, called the single and double escape peaks respectively. In the ^{232}Th spectrum, the peaks with the second and third-highest energy are due to this effect.

2.6 Gamma ray spectrum analysis

A γ-ray spectrum, that is recorded in nature, is composed of γ-rays originating from the decays of mainly ^{40}K, ^{232}Th, ^{238}U and possibly ^{137}Cs. An analysis of the spectrum can determine the amounts of radionuclides in the environment. There is more than one way to do this analysis, but in this research a method will be used called Full Spectrum Analysis (FSA) as described by (Hendriks et al., 2001)[16]. As the name suggests, FSA uses almost the entire γ-ray spectrum for the determination of the radionuclide amounts. This is done by fitting the measured spectrum with standard spectra. A standard spectrum is the response of the detector to a pure source of a radionuclide in a specified measurement geometry at a concentration of 1 Bq/kg. Examples of standard spectra for ^{40}K, ^{232}Th, ^{238}U and ^{137}Cs can be seen in figures 2.1 and 2.2. These standard spectra are then fitted to the measured spectrum using the least squares procedure. The standard spectra are made using Monte Carlo simulations that mimic the measurement geometry.

2.7 Monte Carlo Simulations

This research employs Monte-Carlo simulations to anticipate the response of a gamma-ray spectrometer to γ-rays emitted by various radionuclides in the field. These simulations are used to calculate the standard spectra used in FSA [16] for radionuclide analysis and to evaluate hypotheses about detector and source configurations. The Monte-Carlo simulation samples gamma-ray photons in a specified source-detector configuration and, based on

established nuclear interactions and probabilities, calculates the number of the gamma-rays of a certain energy that reach the detector.

The uncertainty of the simulations is based on the number of γ-rays that interact with the detector. The number of simulated γ-rays generated per second is independent of the volume of the simulation. This means that, assuming the detector size stays the same, the rate at which photons reach the detector decreases proportionally to the size of the simulation. In order to accurately reflect measurement situations, simulations in this research take on a size that has a radius of up to 1.5 km. For models of that size, simulations would have to take a tremendous amount of time to reach a reasonable amount of uncertainty. In order to make it feasible to do these large scale simulations, variance reduction techniques are used. Variance reduction techniques aim to increase the number of γ-rays that reach and interact with the detector per simulated γ-ray, which is the efficiency of the simulation.

2.7.1 Variance reduction techniques

All the Monte Carlo simulations carried out for this research were done using MCNP6™ [17]. MCNP6™ offers several possibilities for variance reduction. These are the ones that were used:

Nested DXTRAN spheres: DXTRAN (deterministic transport) spheres can be used when a small region (such as the scintillation crystal) is being insufficiently sampled due to a low likelihood for particles to scatter in that direction. When a DXTRAN sphere is placed around the detector and particles outside the sphere have a collision, DXTRAN creates a "DXTRAN particle" which is deterministically transported without collision towards the surface of the DXTRAN sphere[18]. The collision itself is also treated normally, creating a non-DXTRAN particle, with no reduction in weight for the normalisation of the simulation. The weight of the DXTRAN particle is scaled to the probability of the original particle to end up at the DXTRAN sphere. By using multiple DXTRAN spheres, the probability for a particle to end up in the detector becomes even greater[11].

Cell importances: When a particle goes from a cell with an importance of 1 to a cell with an importance of 2, MCNP splits the particle track in two, while halving the weight of each track. When a particle goes from a cell with importance 2 to a cell with importance 1 MCNP has a 50 % chance to terminate the particle track, but the weight of the track is doubled. Giving a cell an importance of zero terminates all particle tracks that enter that cell, this is done on the void cell which is the outermost cell to set a boundary on the simulation. By giving the cells close to the detector a higher importance, more of the calculation time is spent on particles in regions where they are of more interest, a normalisation factor based on the weights of the particle tracks is applied to ensure that

the simulation is still representative.

Energy cut-off: Setting an energy cut-off for particles sets a lower limit on the energy for particles. MCNP will stop the calculation for particles that reach this cut-off. This way, less time is spent doing calculations on low energy particles which are not of interest.

Forced capture: This forces the particles inside a cell to have a collision. This can be inside the scintillation crystals to force an event in the detector. This can also be used with DXTRAN spheres to increases the likelihood of them triggering.

Source biasing: Setting a bias such that particles are preferentially emitted towards the detector, can increase sampling efficiency. A correction based on the emission distribution is applied to compensate for the fact that particles are no longer isotropically emitted like they would be in reality.

Chapter 3

Radon corrections

3.1 Radon

Radon, specifically the isotope ^{222}Rn, is a part of the decay chain of ^{238}U. It is a noble gas, so it does not bind chemically to the soil. The half-life of ^{222}Rn is 3.81 days. These properties cause some radon to escape from soil or rock into the atmosphere, where it will eventually decay. The daughters of ^{222}Rn are not gasses, but will bind to aerosols and stay in the atmosphere [19].

The radionuclides that come after ^{222}Rn in the ^{238}U chain include ^{214}Pb and ^{214}Bi, which are the most important γ-ray emitters in the ^{238}U chain. The whole ^{238}U chain emits on average 2.197 γ-rays per decay, the chain after ^{222}Rn emits 2.032. That means that most of the γ-rays are emitted by decays in the decay chain after radon. Figure 3.1 shows the typical response of a detector 80 cm above the ground to ^{222}Rn in the air and ^{238}U in the soil. For both spectra, the activity is set at 1 Bq/kg, and it is assumed that the decay chain is in secular equilibrium. The amount of radiation detected per Bq/kg of ^{222}Rn in air and ^{238}U in the soil is of a similar magnitude. The spectra have peaks at the same energies, with the most prominent peaks at 0.609 MeV and 1.764 MeV. The two spectra are so similar that the γ-ray spectrum of ^{222}Rn in the air is indistinguishable from that of ^{238}U in the ground using current methods.

Geophysical γ-ray surveys aim to characterise the concentrations of ^{40}K, ^{232}Th, ^{238}U in the soil. The presence of ^{222}Rn in the air can lead to a mischaracterization of the ^{238}U concentration in the soil, making it seem higher than it is. This is due to the similar γ-ray spectra and to ^{222}Rn being close to the detector with only air to attenuate its radiation. This causes the signal of radon to be stronger than if it was only present in the ground. γ-ray surveys have been done in the past where the ^{238}U concentration in the soil was inaccurately determined due to this effect [11]. In order to accurately determine the radionuclide concentration ^{238}U in the ground, a correction needs to be applied for the contribution of ^{222}Rn in the atmosphere.

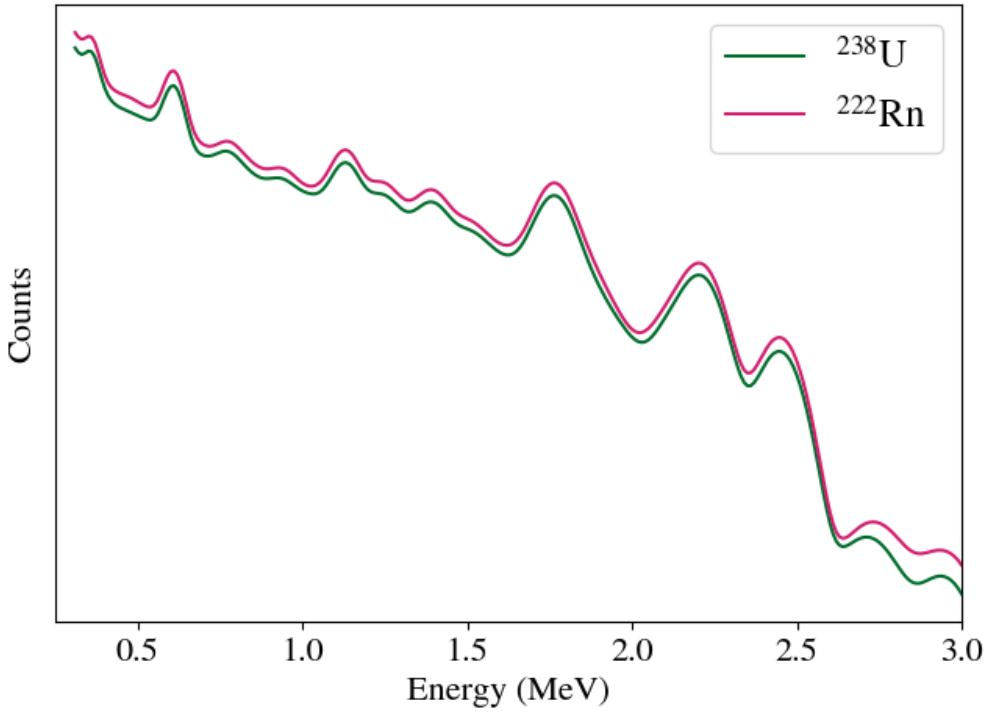

Figure 3.1: The γ-ray spectra of ^{238}U and ^{222}Rn

The decay chain of ^{232}Th also contains an isotope of radon (see Figure 2.2), namely ^{220}Rn, or thoron. This isotope of radon only has a half-life of 56 seconds, which means it does not have enough time to escape from the soil and travel large distances. It is therefore not a concern in geophysical γ-ray surveys. Only ^{222}Rn will be considered for this research.

3.2 Assumptions for radon-correction

In order to correct for the presence of radon in geophysical γ-ray surveys, some assumptions are made that are described in the following three paragraphs.

3.2.1 Secular equilibrium

When radon goes from the ground into the air with lower radon concentrations, it will no longer be in equilibrium. After ^{222}Rn, the decay chain goes through ^{218}Po ($T_{1/2}$ = 3.10 minutes), ^{214}Pb ($T_{1/2}$ = 27.1 minutes), ^{214}Bi ($T_{1/2}$ = 19.7 minutes) and ^{214}Po ($T_{1/2} = 1.63 \times 10^{-4}$ s) until it reaches ^{210}Pb ($T_{1/2}$ = 22.2 years). It takes about five times the half-life of the daughter for its activity to reach 97 % that of the parent, and then it is almost in secular equilibrium. In this case, daughters after ^{214}Bi are ignored because they

are not emitters of γ-rays. The moment secular equilibrium is reached is thus determined by ^{214}Pb and ^{214}Bi, which should be within 3 hours after an increase in the radon concentration in the air.

The assumption of secular equilibrium may not always be accurate. Rainfall can cause the daughters of radon, that are attached to aerosols, to fall down to ground level [19]. This removes the daughters from the air, creating disequilibrium. The simulations in this research and the resulting γ-ray spectra assume secular equilibrium, which means during, or shortly after, rain some radon correction methods can not be applied reliably.

3.2.2 Range of radon contribution

During a geophysical survey, the contribution of radon to the uranium spectrum is determined by the concentration of radon in the air, as well as the volume of the air from which γ radiation reaches the detector. The distance from which radiation from radon reaches the detector can be estimated analytically.

For a sphere of radius R_{max} around the detector, the detection rate of γ-rays (I) is given by [11] chapter 5:

$$I = \frac{A\epsilon\gamma}{2\mu_a\rho_a}(1 - e^{-\mu_a\rho_a R_{max}}) \tag{3.1}$$

Where A is the surface area of the detector, ϵ the efficiency of the detector, γ is the rate of γ-ray production per unit volume of air, μ_a is the mass attenuation coefficient of air, and ρ_a the density of air. In this equation ϵ, γ, and μ_a are all dependent on the energy of the γ-rays. The density of air decreases by about 10 % from sea level to 1000 m height. Using this equation, it was found that at an R_{max} of the sphere of air around the detector of 1000 meters, over 99 % of γ-radiation reaches the detector for both γ-rays of 0.609 MeV and 1.764 MeV (The most prominent peaks in the spectrum) even in the case of 10 % reduced air density. For the sea level air density, 1.225 kg/m^3 was used and the attenuation coefficient 4.447×10^{-3} m^2/kg [20] was used, which is the mass attenuation coefficient for a γ-ray of 2 MeV. μ_a decreases with γ-ray energy, and the contribution is over 99 % at 1000 m which means for 1.764 MeV it will also be over 99 %.

This estimation only uses full energy photons, not photons created in Compton scattering. however, radon only emits a negligible amount γ-rays with energies higher than 1.764 MeV. Therefore, a distance of 1000 meters from radon to the detector is estimated to be the upper limit from where radon contributes to the signal. This estimation relies on a homogeneous radon distribution within a sphere with a radius of 1000 m around the detector.

3.2.3 Spacial and temporal radon variation

Most radon correction methods assume a homogeneous radon distribution in the atmosphere, a constant radon concentration during a geophysical survey, or both. The homogeneity of radon is influenced by its movement in the atmosphere, which has been and still is extensively studied, because radon serves as a tracer for atmospheric transport and mixing processes in climate and pollution studies [21] [22], and because of the health risks associated with radon [23].

The average outdoor radon concentration depends on geographical location. Radon measurements done from 2006 to 2023 at the Lutjewad atmospheric measurement station, located at the northern coast of the Netherlands, average out to 1.78 Bq/m^3 [24]. Radon concentrations in Germany, the United States of America and Japan have been reported to have on average 2 to 23 Bq/m^3 depending on location [25] [26]. Differences in radon level have also been found between urban and rural areas, with larger daily fluctuations in rural areas [27]. At locations where the uranium concentrations are very high, such as uranium mines, radon concentrations in the air have been reported as high as 318 Bq/m^3 [28]. This suggests that the average outdoor radon concentration depends on the local ground uranium concentrations. Close to a large body of water, radon concentrations are influenced by the direction of the wind. This is because the air coming from the sea or large lake contains less radon than air originating from land [29].

Weather conditions are an important factor to consider, as radon concentrations at ground level show variations of up to a factor 20 depending on the weather conditions [30]. During rain, radon-daughters attached to aerosols fall to the ground [19]. This breaks the secular equilibrium of radon in the air and increases the concentration of radon daughters in groundwater [31].

The levels of radon concentration in the atmosphere exhibit daily and yearly fluctuations. With on average larger daily fluctuations happening in the summer [32] [27]. Diurnal fluctuations in radon concentration are thought to be closely linked to atmospheric stability [33]. During the early morning, the atmosphere tends to be stable due to the presence of a temperature inversion, which means that a layer of cold air is trapped under a layer of warm air. A temperature inversion inhibits the movement of radon gas from the ground to the upper layers. Radon concentrations near ground level can increase by up to two orders of magnitude, due to the effect of a strong temperature inversion [34]. This is because radon gas, which primarily originates from the soil, gets trapped at the ground level by the stable atmospheric layer [35]. However, as the sun rises and heats up the ground, the air close to it is heated. This disrupts the temperature inversion, allowing radon gas to disperse into the upper atmosphere [36]. Ground level radon concentrations have been found to negatively correlate with temperature, with a delay of about 3 hours [37] [27]. Wind speed has also been found to negatively correlate with radon concentration [27]. Without wind, mixing in the atmosphere is reduced, as a result radon can accumulate

in the first 1.5 m above ground. This effect can increase concentrations by a factor of four [38].

Variations in radon concentrations can in part be explained by variation in the mixed layer height. The mixing layer is the layer of the atmosphere that is closest to earth's surface. Substances released into the mixing layer disperse slowly in both horizontal and vertical directions due to turbulence, eventually achieving complete mixing given enough time in absence of sources or sinks [39]. Within this layer, potential temperature[1], specific humidity, aerosols, and gasses including radon can be considered homogeneously distributed [29]. The mixing layer height varies between 50 and 2500 m [40] and between 1000 and 2000 m during daytime [41]. When the mixing layer height is under 1000 m, the radon concentration can no longer be considered homogeneous within the volume that influences measurements. However, in 2017. Baldoncini et al. did a study with a γ-ray spectrometer between 70 and 3000 m where they did not observe a sudden change in radon above the mixing layer [42].

γ-ray spectrometers are not able to determine inhomogeneous radon distributions in the atmosphere around the detector. For that reason, radon distribution is assumed to be homogeneous in a plane that extends horizontally around the detector by 10 to 20 km [43]. The distribution of radon in the atmosphere is influenced by various meteorological parameters, making it a complex phenomenon where no single model can fully predict how it influences γ-ray measurements. Nicolet and Erdi-Krausz propose a model that assumes radon is homogeneously distributed for measurements and corrections [2].

The assumption of homogeneously distributed radon may not hold during atmospheric conditions that change the radon concentration. A way to validate the assumption of homogeneity of the radon concentration during a measurement, might be to attach a CO_2 (or another gas) sensor to the detector platform used during a survey. Continuous CO_2 measurements during a survey may be used as a way to test the mixing of the atmosphere. Large fluctuations in CO_2 in the absence of sinks and sources, may indicate a lack of mixing in the atmosphere and thus a radon distribution that is not homogeneous. When atmospheric circumstances are not homogeneous, correction methods may need to be adopted that are specifically designed for such situations. This research will not be concerned with complex radon distributions.

For this research, the distribution of radon in the air is assumed to be homogeneous within a radius of 1000 m around the detector. This is likely a valid assumption during daytime, when it is windy, and when it is cloudy but not raining. Variations of the radon concentration can occur during a measurement, therefore it should be continuously

[1]Potential temperature is a thermodynamic variable used in meteorology and atmospheric science that represents the temperature a parcel of air would have if it were brought to a standard pressure level. It helps to assess the stability and vertical movement of air masses by removing the influence of changes in pressure.

measured during a survey.

3.3 Existing methods for radon-correction

There currently exist multiple methods of correcting for radon in geophysical surveys. These methods are most applicable to airborne gamma ray surveys done with airplanes and helicopters, with some being viable for ground-borne surveys as well. These platforms offer the ability to carry heavy loads in excess of 100 kg. Airborne surveys are typically done with γ-ray spectrometer systems consisting of a minimum of 4 times 4 litre NaI crystals, up to sixteen 4 litre NaI crystals [2]. Radon correction models can be separated into two categories, separate radon measurements and spectral correction methods.

3.3.1 Independent radon measurements

With these methods, a separate radon measurement is done, which is then used to make corrections to survey data.

Taking air samples

The concentration of radon in air samples taken during the survey is determined by using a radon detector, with the analysis mainly relying on the detection of alpha particles emitted by radon and its decay products [11].

Calibration flights over large bodies of water

Radon corrections can be done by performing a calibration flight above water [44] [2]. Given the low radionuclide concentration in water, the gamma-radiation emitted by it can be disregarded. For this technique to be effective, the water layer must be at least 1 meter thick [45], and the measurement platform must be shielded by 200 to 500 meters of air between the shore and detector. This provides adequate shielding for gamma-rays emitted by the underlying geology and the surroundings [11]. As a result, all counts recorded must originate from cosmic rays or radon. This method can only be applied if there is a large body of water next to the survey area.

Upwards looking detectors

A detector pack containing multiple crystals is augmented with an extra detector placed on top. Shielded by the high-density detectors below, this additional detector registers events primarily caused by gamma-rays produced by cosmic rays or radon above the main detector [2]. Throughout the survey, the count rate due to cosmic rays remains steady, and it is assumed that the count rate recorded by the upward-looking detector correlates linearly with the count rate contributed by radon in the downward-looking detectors. Upwards looking detectors can be calibrated by doing calibration flights above water [44] or land [46].

3.3.2 Spectral correction methods

The objective of these techniques is to extract the radon component within the measured spectra, without requiring any supplementary equipment to determine the concentration of radon. The spectral correction methods use the fact that gamma-rays from the ^{238}U decay chain are formed in the ground and subsequently attenuated by the ground and the air. Gamma-rays resulting from the decay of ^{222}Rn are generated in the air around the detector and therefore only attenuated by the air. The gamma radiation originating in the air is attenuated less. The result is that spectra of uranium and atmospheric radon exhibit similar shapes at 1.76 MeV. However, at 0.609 MeV, the uranium spectrum will have a smaller peak-to-Compton ratio than that of radon [43].

Spectral ratio method

In this approach, the existence and impact of radon are determined by evaluating the ratio between two peaks emitted by ^{214}Bi: one at 0.609 MeV and the other at 1.76 MeV [44]. In this method, the height of the peaks above the Compton continuum is used, rather than the peak's full height. As gamma-ray spectrometers have evolved to offer greater resolution, this technique has been broadened to encompass the ratio between the 0.352 MeV peak from ^{214}Pb and the 1.76 MeV peak [47]. This method has also been applied to in UAV-borne surveys [48].

Full spectrum method

This approach is comparable to the spectral ratio method, but instead employs the complete spectrum to identify the existence and impact of radon [44] [45] [49].

3.3.3 Application of radon correction methods

All of these methods require a calibration to map the measured quantity to the concentration and obtain a spectrum that can be subtracted from spectral measurements. Calibration methods have traditionally been based on empirical approaches [10] [2], but in recent times, Monte Carlo methods are being employed to model the detector response [47] [50]. Upwards looking detectors and air sampling to correct for radon levels requires extra equipment. Air sampling and calibration flights assume that there is a partial spatial and temporal homogeneity in the radon concentrations.

Upward looking detectors, spectral ratio, and full spectrum correction methods do not assume a homogeneous distribution of the radon concentration throughout the survey area. However, it is important for these methods to have well-defined spectra. When using a 16 litre NaI crystal pack, integration times of 200 to 600 seconds are typically necessary to collect sufficient counts for applying corrections [2]. For airplanes, typical survey speeds are 50-60 m/s, resulting in the summation of data over 10-36 km, while for helicopters, speeds

are 25-30 m/s, resulting in the summation of data over 5-18 km [2]. It should be noted that although these methods do not assume a homogeneously distributed concentration throughout the survey, they assume such a distribution over the area where the data is summed.

3.3.4 Limitations of spectral correction methods

In order to apply the spectral ratio or full spectrum method, it is required to characterise the differences between the ^{222}Rn and ^{238}U spectrum. This requires a few conditions to be met.

Firstly, the ^{222}Rn and ^{238}U spectra need to be distinct enough from each other to see a difference. Since the difference in the spectra is caused by the difference in attenuation, this requires sufficient measurement height [11].

Secondly, It is preferred that ^{137}Cs is not present. Mainly in the Northern Hemisphere, ^{137}Cs entered the environment as a result of nuclear bomb tests and accidents from the nuclear power industry. ^{137}Cs emits γ-rays of 0.662 MeV, which interferes with the 0.609 MeV peak used in the spectral ratio method. NaI or CsI detectors commonly used in geophysics have a 7-10 % resolution [2]. This resolution limits the ability to differentiate between the 0.609 and 0.662 MeV peaks. The distinction can only be made when there is a sufficiently high concentration of ^{137}Cs, and enough counts are obtained to ensure both peaks are well-defined. Despite the limitations of the spectral ratio method when using the 0.609 MeV peak in the presence of ^{137}Cs, the method can still be applied using the 0.352 MeV peak. Additionally, the full spectrum method can be utilized, provided that a standard spectrum for ^{137}Cs is included. [11]

Finally, it is necessary to determine the effect of radon on the measurements. The measured radon concentration in the air must be converted to a parameter that can be used to adjust the data. This can be achieved by multiplying a pure radon spectrum by the concentration, which is then subtracted from the measured spectra, or by applying a correction factor for the uranium concentration. The radon spectrum or correction parameter can be determined through measurements or Monte-Carlo simulations. However, it is important to note that both methods rely on certain assumptions about the temporal and spatial variations in radon concentration during the survey. [11]

3.4 UAV-borne methods for radon-correction

The correction methods presented so far have mainly been designed for, and applied in, airborne γ-ray surveys. Compared to airplanes and helicopters, UAVs typically carry a much lighter load, fly at lower altitude for a shorter time covering a smaller area during a

survey. These differences will affect the applicability of some radon correction methods described in the previous section. This section will cover the applicability of these methods to UAV-borne γ-ray surveys as well as two new radon correction methods, proposed in the work of S. van der Veeke [11], which have been specifically designed for UAV-borne γ-ray surveys.

Due to limited payload on UAV-borne gamma-ray surveys, an upward-looking detector cannot be effectively used as smaller detectors are typically used which provide limited shielding. Moreover, maximising the crystal volume for the actual measurement is preferred. Therefore, no, or only a small separate upward-looking detector can be used on a UAV.
The use of calibration flights above water for UAV-borne surveys require a body of water close to the survey area. UAV flights cover a smaller area than airborne surveys, and there may not be a body of water of adequate size within the survey area. UAVs require smaller distances from shore than is necessary for airborne surveys, because they can fly close to the water surface. This means smaller bodies of water may be used for the calibration flight if the UAV operator is able to bring their UAV very close to the water. This however requires that the body of water is not located in a valley where the surrounding terrain extends far above the water level and contributes to the γ-ray spectrum. In conclusion, calibration flights can be a viable method for radon correction, but only situationally as it requires certain geographic conditions in the survey area.

Because UAV-borne γ-ray surveys are typically performed at a lower altitude compared to the traditional airborne surveys, the γ-rays are attenuated less before reaching the detector. While this allows for the use of smaller detectors, it also means that the spectral ratio or full spectrum method become more difficult to use because these methods rely on the difference between the attenuation of the γ-rays from ^{222}Rn and ^{238}U. This difference is reduced at lower altitude. Despite this, advanced spectral-ratio radon background correction methods have been used to perform radon corrections with a UAV [48]. This was done with a 4 litre NaI (Tl) crystal with a weight of 19.8 kg, which requires a UAV capable of carrying this weight.

3.4.1 Radon corrections based on measurements at different heights

This method uses the ability of UAVs to hover in place precisely at a fixed altitude and the intensity of radiation from uranium as a function of height. The intensity of the radiation due to uranium and radon for a specific energy γ-ray as a function of height is given by [11]:

$$I_{total}(h) = (I_0^U - I_0^{Rn})E_2(h\mu_a\rho_a) + 2I_0^{Rn} \tag{3.2}$$

Where I_{total} is the intensity of the combined radon and uranium spectrum, h is the height of the detector,I_0^U and I_0^{Rn} are the intensity due to uranium and radon respectively at zero

height. μ_a and ρ_a are the mass attenuation coefficient and density of air respectively, and E_2 represents the exponential integral of order two [51]. The contribution to I_{total} from uranium decreases with height, while the contribution of radon increases.

By performing measurements at several heights, it is possible to fit the curve from equation 3.2. This curve is shown in Figure 3.2 for three situations. The blue curve indicates what the detector is predicted to measure ($I_{total}(h)$), the red and green line represent the signal due to ^{222}Rn and ^{238}U respectively. Because it is known how the signals from ^{222}Rn and ^{238}U change with height, the ratio of ^{222}Rn and ^{238}U can be determined from a characterisation of the total signal as a function of height.

It is assumed that the uranium concentration is constant within the footprint of the

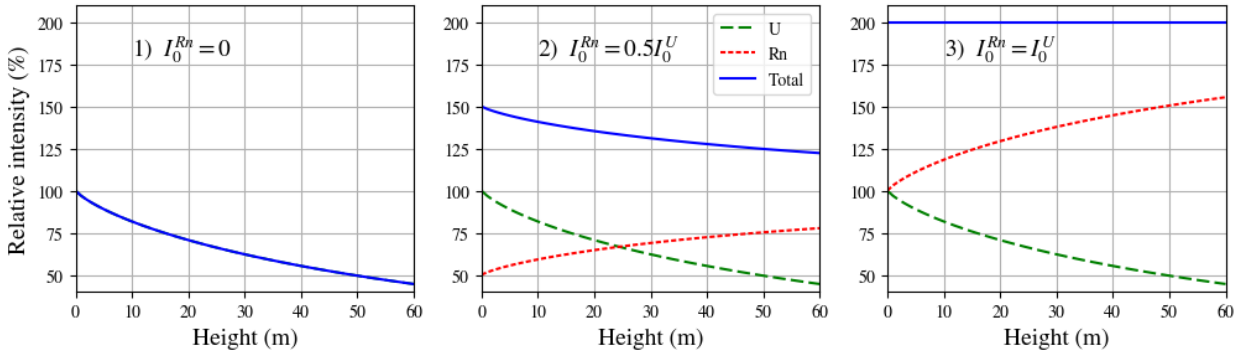

Figure 3.2: The intensity of the 1.76 MeV full energy peak due to ^{238}U (green) in the ground, ^{222}Rn (red) in the air and their sum (blue). In graph 1, no radon is present, as a result the uranium signal (green) and the total (blue) overlap. In graph 2, The intensity due to radon at ground level is half that of uranium, the total signal decreases slower than in graph 1. In graph 3, the intensity due to radon at ground level equals that of uranium. In this situation, the total signal is constant with height. This figure was recreated from [11].

measurement for equation 3.2. The footprint is the area underneath the detector that influences the measurement, the size of the footprint increases with height [11]. In Figure 3.2, $I_{total}(h)$ is plotted for different values of I_0^U and I_0^{Rn} using equation 3.2. For graph 1 $I_0^{Rn} = 0$, in this situation, the intensity of the total signal decreases the fastest. For graph 3, $I_0^{Rn} = I_0^U$ and as a result, the total signal remains constant.

With measurements at different heights, only the ratio between ^{222}Rn and ^{238}U can be determined. In order to find the absolute concentrations a supplementary method has to be used, such as taking air samples, soil samples or the spectral ratio method. In the curves shown in Figure 3.2, purely the attenuation of gamma-rays of a specific energy is considered and not other physical effects such as Compton scattering and pair production. Monte Carlo simulations can incorporate these effects and help to determine the intensities as a function of height.

3.4.2 Radon detection using a split γ-ray spectrometer [11]

This method of radon correction takes the principle of the upwards looking detector, and integrates this into the detector design so that it also contributes to the measurement of ground radionuclides. This method depends on the characterisation of the detector by Monte Carlo simulations. Figure 3.3 shows a possible design of a split detector. The

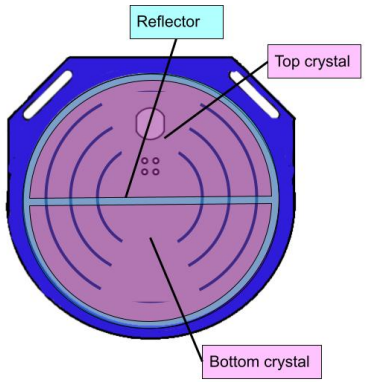

Figure 3.3: A schematic image of the split detector. The magenta indicates how the scintillation crystals are placed inside the detector. On the top of the detector mounting points are added, which can be used to attach the detector to a UAV

detector is composed of a scintillation crystal which is split into two parts which are separated by a thin layer of reflective foil, the same material that is used outside surface of the scintillation crystal to reflect scintillation photons back into the crystal in order to increase the probability of them ending up in the photo-multiplier. In this design, both crystals are equipped with their own photo-multiplier and multichannel analyser. As a result, the detector outputs two signals, one for the top crystal and one for the bottom crystal.

When performing a measurement with this detector with it oriented such that the top crystal is pointed upwards, the top crystal will be partially shielded from radiation that is coming from below and the bottom crystal is partially shielded from radiation from above. Consequently, more of the radiation coming from ^{238}U and other nuclides in the ground will be detected by the bottom crystal and more of the radiation due to ^{222}Rn in the air will be detected by the top crystal.

To determine the levels of ^{40}K, ^{238}U, and ^{232}Th in the soil, the combined signal from both halves is utilized. The measured spectra can have their ^{40}K and ^{232}Th contributions subtracted, and the total count of the upper and lower crystals can be analysed independently. Monte-Carlo simulations are used to calculate and calibrate the responses of the detectors to ^{238}U from the soil and ^{222}Rn in the air for each detector, using the methods described in [50]. With the crystal sizes typically employed in geophysical surveys, the photon shielding between the two halves is only partial. Nonetheless, this approach is

practical as long as the shielding is strong enough to produce a distinguishable difference in count rate between the two crystal halves, depending on the source of the radiation.

The total number of counts due to the combined signal of ^{238}U in the ground and ^{222}Rn in the air in the top crystal (I_T) and bottom crystal (I_B) are given by:

$$\begin{aligned} C^U \eta_T^U + C^{Rn} \eta_T^{Rn} &= I_T \\ C^U \eta_B^U + C^{Rn} \eta_B^{Rn} &= I_B \end{aligned} \tag{3.3}$$

Where C^U and C^{Rn} are the concentrations of ^{238}U and ^{222}Rn respectively in Bq/kg. η indicates the number of counts per Bq/kg registered due to ^{238}U and ^{222}Rn, superscript U and Rn respectively, in the top and bottom crystal with subscript T and B respectively. Equations 3.3 can be rewritten to:

$$\begin{aligned} C^U &= \frac{\eta_T^{Rn} I_B - \eta_B^{Rn} I_T}{\eta_T^{Rn} \eta_B^U - \eta_B^{Rn} \eta_T^U} \\ C^{Rn} &= \frac{\eta_T^U I_B - \eta_B^U I_T}{\eta_T^U \eta_B^{Rn} - \eta_B^U \eta_T^{Rn}} \end{aligned} \tag{3.4}$$

That means that after measuring I_T and I_B, both the ^{238}U and ^{222}Rn concentrations can be calculated. The values for η are determined in Monte Carlo simulations.
Equations 3.3 and 3.4 can also be rewritten with the following substitutions:

$$\begin{aligned} \eta_T'^U &= \frac{\eta_T^U}{\eta_T^U + \eta_B^U} \\ \eta_B'^U &= \frac{\eta_T^U}{\eta_T^U + \eta_B^U} \\ \eta_T'^{Rn} &= \frac{\eta_T^{Rn}}{\eta_T^{Rn} + \eta_B^{Rn}} \\ \eta_B'^{Rn} &= \frac{\eta_T^{Rn}}{\eta_T^{Rn} + \eta_B^{Rn}} \\ C'^U &= C^U(\eta_T^U + \eta_B^U) \\ C'^{Rn} &= C^{Rn}(\eta_T^{Rn} + \eta_B^{Rn}) \end{aligned} \tag{3.5}$$

Where we now have relative efficiencies $\eta_T'^U(\eta_T'^{Rn})$ and $\eta_B'^U(\eta_B'^{Rn})$, which are the fraction of the total counts due to uranium (radon) in the top and bottom crystal respectively and $C'^U(C'^{Rn})$ the total number of counts due to uranium (radon).
A prototype was built of this detector, henceforth referred to as "the split detector". Using the split detector as a means to correct for atmospheric radon in geophysical surveys will be the main focus of this research.

Chapter 4

The split detector

4.1 Introduction

In order to test if the split γ-ray spectrometer method can be used to measure and correct for the radon concentration in the atmosphere, a prototype was built. In this chapter, this prototype will be described. Then the calibration procedure is described, which involves a measurement in a calibration setup. The split detector is capable of detecting whether radiation is isotropic within the calibration setup, this was tested and documented in this chapter as well.

4.2 The design of split detector

The prototype of the split detector is displayed in Figure 4.1. The two scintillation crystals were made out of a 1 litre cylindrical CsI crystal of 160 mm high and 90 mm in diameter. This makes the weight of the detector similar to that of the MS-1000 from Medusa Radiometrics, which is made for UAV-borne survey applications[52]. The crystal was divided into two half cylinders which are separated by reflective material. The crystals are made from the inorganic scintillation material CsI, for its durability and resolution, as is described in 2.5. At the end of the two crystals, silicon photo-multipliers are used to collect the light from the crystals. These silicon photo-multipliers are placed inside a potting compound to keep them in place alongside an amplifier which amplifies the signal from the silicon photo-multipliers. The CsI crystals, silicon photo-multipliers, amplifier and potting compound are all inside an aluminium housing.

The aluminium housing with the crystals is placed inside a carbon fibre tube, separated by a layer of foam for shock-absorption. On one end of the carbon tube, the electronics of the detector can be found. This includes two multichannel analysers with 512 channels, to acquire the spectra used in the determination of radionuclide concentrations. Among the electronics a pressure, temperature, and humidity (PTH) sensor is included in order to be able to make corrections for the small temperature dependence of the detector[50]. Among

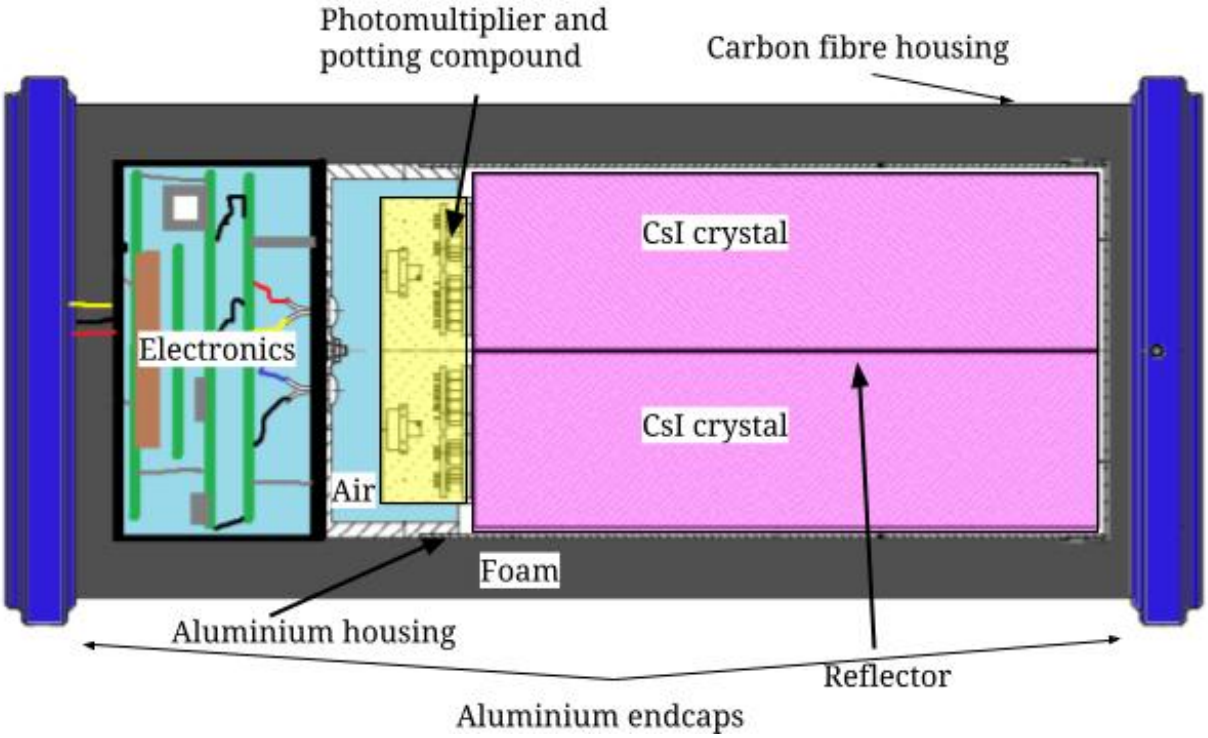

Figure 4.1: Schematic cross-section of the split detector.

the electronics is also the computer system that runs mDOS (Medusa Detector Operating System). mDOS provides a standardised web interface to the detector system, which allows set-up and check of system parameters and system functioning. The electronics of the detector connect through a connector in the aluminium end-cap. Via this connector power, Ethernet and GPS can be connected to the detector. The end-caps of the detector have mounting points which can be used to securely attach the detector to a UAV. These mounting points can be seen in Figure 3.3 are on the top-side of the detector

4.3 The calibration of the split detector

In order to use a γ-ray spectrometer to determine the ground radionuclide concentrations, it first needs to be calibrated. A Monte Carlo based calibration method is used, described in detail by van der Graaf et al., 2011 [50]. The calibration of the split detector required Monte Carlo simulations, and measurements to be done inside a calibration setup. Medusa Radiometrics has a dedicated calibration setup called "Stonehenge" which is shown in Figure 4.2. Stonehenge is a 1.2 by 1.2 by 1.2 m structure made of clay bricks which have a well known activity concentration of ^{40}K, ^{238}U and ^{232}Th. It is large enough to ensure that 99.9 % of radiation detected by a detector comes from Stonehenge, and only 0.1 % from

Figure 4.2: The Stonehenge calibration setup[54]

the walls and floor around it[53].

The split detector has directional sensitivity, which means it can measure if the radiation in Stonehenge is isotropic. Ideally, the direction of radiation within Stonehenge in both simulations and reality is the same, that way the two are comparable. This is considered in both the simulations and the measurements that were done inside the setup.

First, the simulations of the split detector inside Stonehenge are described. Thereafter, the measurements are presented and discussed.

4.3.1 Stonehenge simulation

In the calibration procedure, the first step is to perform Monte Carlo simulations of the split detector in the calibration setup. For this, Stonehenge was recreated in MCNP6™, the program used for Monte Carlo simulations. The geometry of the simulation is shown in Figure 4.3. For each radionuclide, a simulation was done with the bricks from Stonehenge acting as a source of ^{40}K, or the decay chain of ^{238}U or ^{232}Th in secular equilibrium. In the simulations, the bricks were assumed to be pure SiO_2 with a density of 2320 kg/m^3. Air was taken as a mixture of N_2 (79 % mass) and O_2 (21 % mass) with a density of 1.293 kg/m^3. In order to simulate the response of the detector, the MCNP6 pulse height tally (F8-tally) was used. This tally is capable of estimating the energy spectrum in a physical detector model.

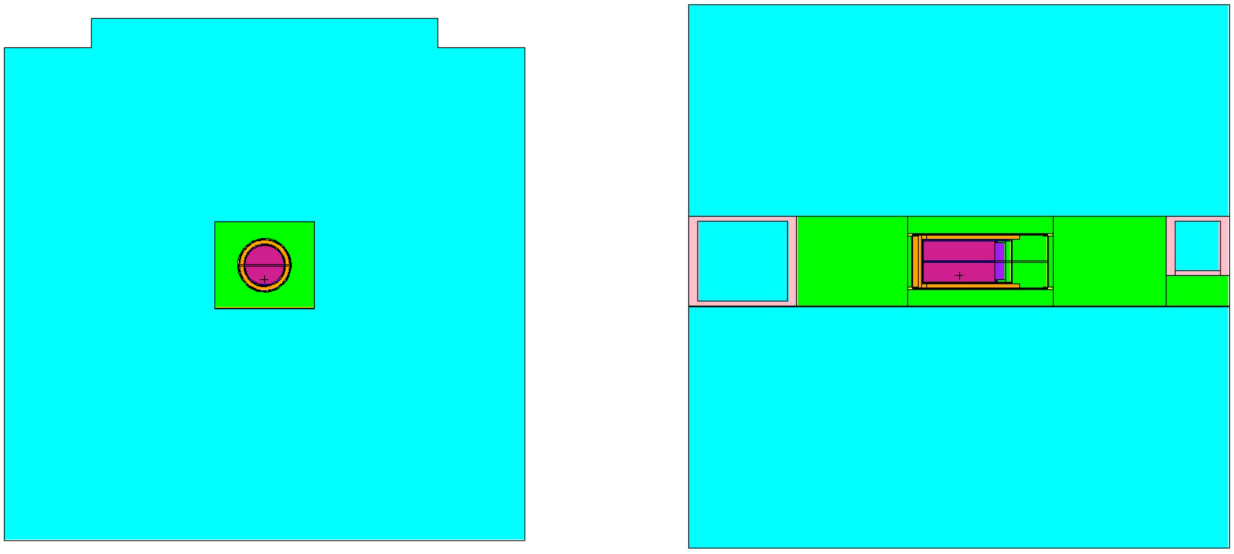

Figure 4.3: The geometry of the simulation of the split detector in Stonehenge. The left image is a front view, and the right a side view. The detector is located in the centre, with air around it in green. The bricks from Stonehenge are shown in cyan.

Results from the Stonehenge simulation

The main results of the simulation in Stonehenge are the detector response curves to a 1 Bq/kg source of each ^{40}K, ^{238}U and ^{232}Th for each crystal. These response curves represent the spectrum one would measure in the situation of a tool inside a Stonehenge-type geometry having an activity of 1 Bq/kg. The spectra produced by Monte Carlo simulations are an unbroadened histogram, as in figure 4.4. In the calibration procedure, these are broadened using a Gaussian broadening function to match the resolution of the detector.

Stonehenge fully surrounds the detector and made of clay bricks, which should all be roughly identical. If the radiation in Stonehenge is isotropic, there should be no difference between the crystals. Table 4.1 presents the total number of counts per second per Bq/kg for each radionuclide determined in the simulations. The top crystal receives 0.7 ± 0.1 % more radiation than the bottom crystal for ^{238}U and ^{232}Th, and 0.4 ± 0.1 % more radiation for ^{40}K.

	Top crystal (Cps/Bq/kg)	Bottom crystal (Cps/Bq/kg)	Difference (%)
K	0.6090±0.0004	0.6068±0.0004	0.4± 0.1
U	9.842±0.007	9.770±0.007	0.7± 0.1
Th	11.763±0.009	11.689±0.009	0.7± 0.1

Table 4.1: Total counts per Bq/kg in the energy range from 0 to 3 MeV, calculated from Monte Carlo simulations inside Stonehenge.

4.3.2 Stonehenge measurements

The next stage of the calibration procedure is a measurement with the split detector in the Stonehenge calibration setup. The two spectra, measured by the detector halves, are then energy stabilized, normalized and approximated by the Monte Carlo calculated standard spectra. This procedure involves the following steps:

- Determination of a function that maps "raw" multichannel spectral data to an energy-calibrated spectrum. This procedure involves determining the function required to convert a channel in the MCA spectrum into its corresponding energy value in the energy spectrum. To accomplish this, a quadratic mapping function is employed, characterized by three parameters: a_0, a_1, and a_2. The a-factors represent the coefficients of a second-order function that converts channel numbers into energy values.

  1. a_0 denotes the channel offset within the multichannel system.
  2. a_1 represents the linear scaling factor, which is dependent on temperature.
  3. a_2 represents a quadratic correction to the scaling of channel numbers to energy values.

- Determination of the spectral resolution of the detector by broadening the unbroadened histograms, from the Monte Carlo simulations, to match the detector's spectral resolution.

- Determination of a general scaling factor that quantifies the disparity between the theoretical detector response and the actual response. Where the theoretical response corresponds to what the simulations predict given the known radionuclide concentrations in Stonehenge, which are 41 Bq/kg ^{238}U, 52 Bq/kg ^{232}Th and 535 Bq/kg ^{40}K.

- Converting the calibration geometry to the geometry in which the detector is meant to be used. This is achieved by doing simulations of the detector in the geometry where it is intended to be used. In this case, that geometry is the split detector in its intended orientation above a flat field of radionuclides.

These steps are outlined in detail in van der Graaf et al. 2011, [50]. The calibration procedure yields a collection of standard spectra, which can be used in Full Spectrum Analysis for the examination of gamma ray data obtained in field measurements. The output of the calibration procedure is a Medusa Calibration File (MCF), designed to be used in the Medusa spectral analysis software.

The crystal that is on top, when the detector is oriented right side up (as in Figure 5.1A), is named crystal 1 and the other is crystal 2. This is to avoid any confusion as to which crystal is being discussed. For the calibration measurement, the detector was placed inside Stonehenge (see Figure 4.2) and spectra were acquired with detector 1 on top (measurement time 94 minutes) and detector 2 on top (measurement time 41 minutes).

Results

Before any calibration procedure, one can already look at the total counts per second in each crystal. The results are in Table 4.2. Crystal 1 had a higher count rate than crystal 2 in both the right side up and upside down orientations. For both crystals, the count rate was higher if it was looking down.

Crystal	Facing up	Facing down
1	753.2±0.4	765.1±0.6
2	706.4±0.6	711.6±0.4

Table 4.2: Total counts per second of each crystal when looking up and when looking down

The spectra, that were measured with crystal 1 facing up and crystal 2 facing down, were used to determine the calibration parameters using the standard spectra determined in the simulations. The fit of crystal 1 can be seen in Figure 4.4. In this fitting procedure, the factors a_0, a_1, and a_2, the resolution and the overall scaling factor were determined for both crystals. The parameter a_2 was kept at 0 for both crystals while retaining a good fit. These parameters can be seen in Table 4.3.

Parameter	Crystal 1	Crystal 2
a_0	-4.20	-5.00
a_1	0.665	0.673
a_2	0.00	0.00
Energy resolution	8.3%	8.7%
Overall scaling factor	99.4%	93.0%
Energy range (MeV)	0.36-2.72	0.36-2.72

Table 4.3: The parameters that were determined from the calibration procedure. With a_0, a_1 and a_2 being the parameters of the function that maps MCA channels to their corresponding energy. The energy resolution is the FWHM as a percentage of the peak energy at 0.662 MeV. The Overall scaling factor is the amount of radiation detected compared to the theoretical value in the energy range that is given below it.

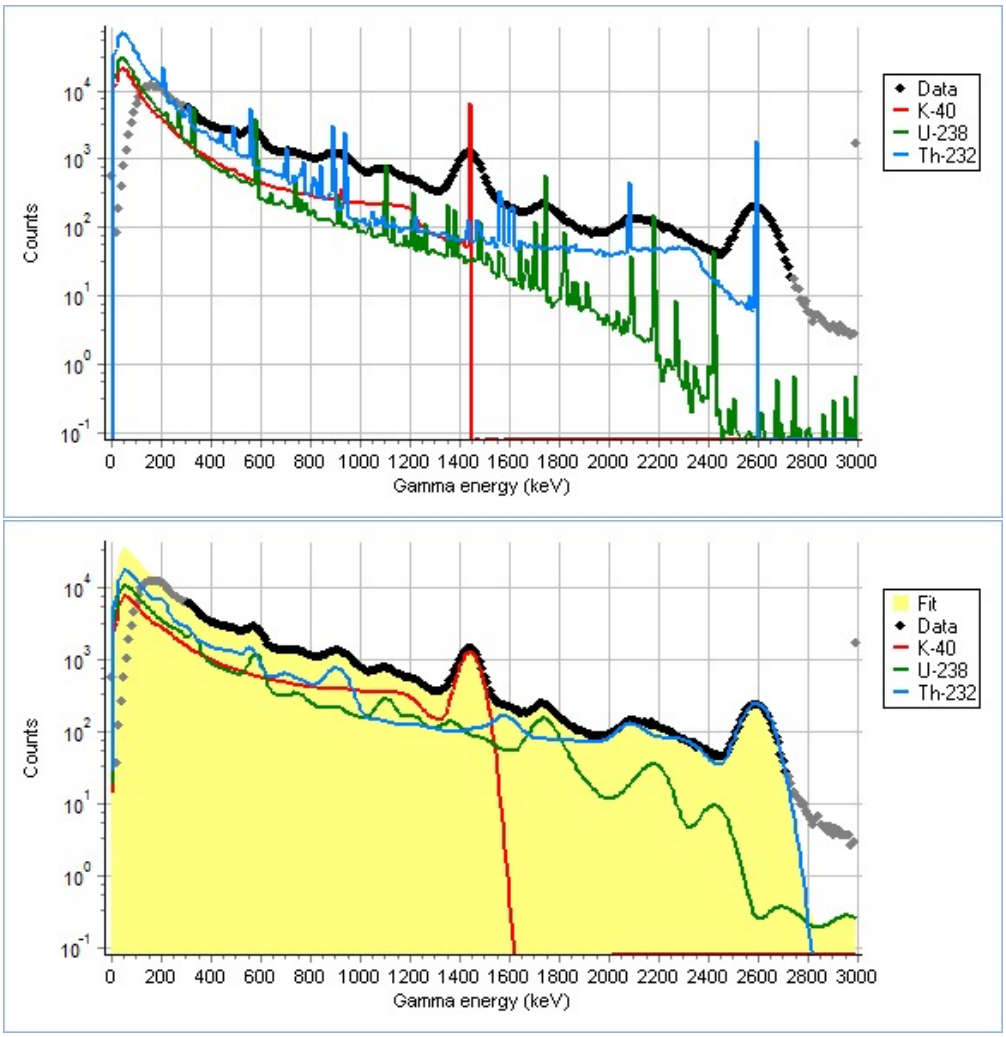

Figure 4.4: The raw spectrum measured by crystal 1 in Stonehenge (black and grey dots). With on the x-axis, the energy of the γ-rays and on the y-axis the total counts on a logarithmic scale. With on top the unbroadened histograms of ^{238}U (green) and ^{232}Th (blue), and ^{40}K (red) from the Monte Carlo Simulations, and on the bottom the histograms broadened to match the resolution of the detector of 8.3 %. These pictures were made using the MCF creator, which is the computer program developed by Medusa to create calibration files.

4.3.3 Geometry conversion

The final step in the calibration procedure is the conversion of the geometry from Stonehenge to the geometry in which the split detector is intended to be used. The geometry that is used in this case is a flat field with the detector floating above it, this is shown in Figure 4.5. This geometry is referred to as the flatbed geometry. The flatbed consists of stacked circular discs of soil modelled as SiO_2 1500 kg/m^3 with 300 kg/m^3 H_2O. The radius of the discs decreases with depth, and the thickness increases. This shape was chosen because it approximates the volume of ground that contributes 99 % of the

radiation that reaches the detector when it is at heights of 10 m to 40 m[11]. For simulations with the detector at 0.8 m height, a smaller flatbed was geometry used with a maximum radius of 68 m. This was done because simulations with a 450 m radius flatbed produced results with uncertainties that did not seem to get smaller with simulation time at this height. However, at this detector height, a flatbed of this size should still be responsible for 99 % of the radiation that reaches the detector[11].

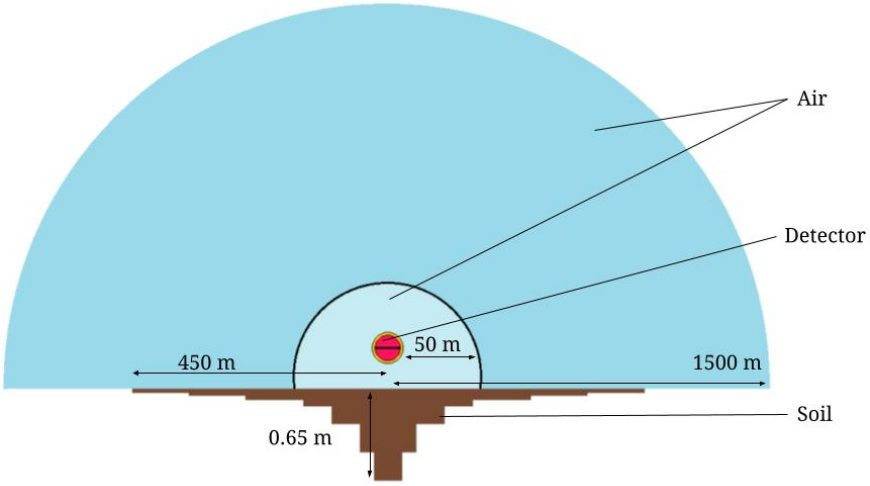

Figure 4.5: Schematic picture of the flatbed geometry, not to scale. For simulations with the detector at 10 m or higher, the soil consists of a stack of discs of radius 450, 350, 250, 150, 100, 50 and 25 m from top to bottom, with a thickness of 0.03, 0.02, 0.03, 0.045, 0.125, 0.20 and 0.20 m respectively. The maximal depth of the soil was 0.65 m underneath the detector. The entire soil was used as a ^{40}K, ^{238}U, ^{232}Th and ^{137}Cs source. For the simulations of radionuclides in the ground, only the air up to the edge of the widest soil disc was used. For ^{222}Rn, air around the detector is a half-sphere of 1500 m within which is a sphere with a radius of 50 m around the detector. Separate simulations were done with the inner 50 m and the rest of the air acting as a ^{222}Rn source.

The soil was used as a ^{40}K, ^{238}U, ^{232}Th and ^{137}Cs source. For every radionuclide, a separate simulation was run at a height of 0.8 m and 10 m. The response curves resulting from these Monte Carlo simulations were then used to create the standard spectra, and Medusa Calibration Files such that the split detector can be used for radionuclide measurements.

Radon simulations

In order to use the split detector as a correction method for ^{222}Rn. The efficiencies from 3.4 of the crystals had to be determined. To do this, Monte Carlo simulations were done with ^{222}Rn in the air. The ^{238}U simulation results from the geometry conversion were used to calculate η_B^U and η_T^U.

The simulations with ^{222}Rn in the air were done in 2 parts, one with ^{222}Rn in the first 50 m of air around the detector and one with ^{222}Rn in air except in the first 50 m around the detector. In the simulation of the inner sphere of ^{222}Rn, the outer layer of air and the soil were removed from the simulation with the assumption that the contribution of photons that travel there and scatter into the detector is negligible. The spectra resulting from the two simulations of ^{222}Rn were summed to create a single combined spectrum. The reason ^{222}Rn was simulated in two parts was to speed up simulations, as doing this produced results quicker than simulating radon in one go. For these simulations, several variance reduction techniques were used. Namely: Nested DXTRAN spheres, Cell importances, forced capture source biasing and the energy cut-off for photons was set at 0.1 MeV.

The results of these simulations for the various η's at a height of 0.8 m and 10 m are shown in Table 4.4. The total counts due to ^{238}U and ^{222}Rn were being higher for the simulation at 10 m than the simulation at 0.8 m.

	$\eta_B'^U$ (%)	$\eta_T'^U$ (%)	$\eta_B'^{Rn}$ (%)	$\eta_T'^{Rn}$ (%)	U (counts per Bq/kg)	Rn (counts per Bq/kg)
0.8 m	60.7±0.4	39.3±0.4	40.4±0.2	59.6±0.2	1.93±0.02	2.42±0.01
10 m	60.1±0.5	39.9±0.5	42.3±0.5	57.7±0.5	2.09±0.02	2.56±0.02

Table 4.4: The efficiencies and the total counts per second per Bq/kg of the split detector in the flatbed geometry at 0.8 m and 10 m height in the energy range 360 keV to 2720 keV.

4.4 Discussion and Conclusion

This chapter provided a description of the split detector design and the calibration procedure. The calibration of the detector involved a combination of Monte Carlo simulations and measurements conducted at Stonehenge. Ultimately, standard spectra were generated through Monte Carlo simulations conducted in a flatbed geometry.

The measurements in Stonehenge revealed that crystal 1 detected more radiation than crystal 2 in both orientations of the detector. One possible explanation for this is, that crystal 1 and crystal 2 have a slightly different size. They were once a single crystal that was sawed in half, if the cut was made slightly off-centre this would result in crystals of different sizes. A difference in size could impact the values of the various η's from equation 3.4. This was not looked into further because there was no way to simply disassemble the detector to determine the exact shape and size of the crystals.

In the simulations of the split detector inside Stonehenge, it turned out that the top crystal received slightly more radiation than the bottom crystal. This is possibly due to the aluminium plate that is on the bottom of the cavity in Stonehenge. In the measurements with the split detector inside Stonehenge, the opposite seemed to be true because both

crystals had a higher total count rate when pointed down. Crystal 1 and crystal 2, respectively, recorded 1.6 % and 0.7 % more total counts when looking down than when looking up. This could be due to a slight asymmetry in Stonehenge and due to the fact that it is not a 100 % shielded environment. In the surroundings of Stonehenge, more radiation might come from below than from above. If the shielding provided by the bricks is not 100 % that will show up in the measurement that was done.

Although there was a difference observed between the measurement and simulation, the calibration of the detector was performed using the measurement obtained from crystal 1 in an upward orientation. This decision was made because the disparity between a crystal facing upward and one facing downward is only around 1 %. This small difference should not hinder the split detectors' capacity to compensate for the presence of radon during geophysical surveys. In the simulation, the crystal that was facing upward (or downward) was paired with crystal 1 (or 2) respectively, and an MCF was generated for each crystal. This ensured that both crystals were prepared and ready for deployment in field measurements.

If it turns out from the field measurement that there is a discrepancy between the radionuclide concentrations determined by the top and bottom crystal. That might be due to the differences encountered between measurement and simulations in Stonehenge, with the crystals facing vertical directions. It may be a good idea to redo the calibration, with the simulations and measurements done with the crystals facing horizontal directions.

Chapter 5

Rotating the split detector

5.1 Introduction

Unlike other γ-ray spectrometry systems, the split detector is build to be sensitive to the direction γ-rays are coming from. In the intended orientation, the split detector has one crystal looking up, and one crystal looking down. However, if the detector is rotated about either its x-axis or its z-axis, as illustrated in Figure 5.1, the two detector halves will now be looking up and down along some rotated y'-axis. This could be an important source of systematic error, during γ-ray surveys. Especially if this detector is to be used under a UAV, which can pitch forward during forward flight, the pitch angle is dependent on the velocity of the UAV[55]. Flights have been recorded with a forward pitch of around 15° to 20° for most of the flight[56].

Under a UAV, the x- and z-axes about which the detector is rotated are not necessarily centred, as in Figure 5.1. If that happens, a translation of the detector accompanies the rotation, possibly altering its height. As long as the displacement of the axis of rotation and the angle of rotation are small, the vertical displacement caused by this effect is also small. For this chapter, the focus will be on the effect of rotations rather than small detector height fluctuations.

If the split detector is to be used to measure radon, it should be known how much its rotation affects measurement results. During measurements, one could make sure that the detector stays aligned within a certain tolerance such that the effect of rotations can be neglected, in the latter case the tolerances of the detector need to be determined. Alternatively, one can monitor the angles of the detector during use and apply a correction to the measurement accordingly. In which case, the angular dependence of various parameters should be determined. In this chapter, the dependence of the efficiencies η_B^{Rn}, η_T^{Rn}, η_B^U, η_T^U of the crystals will be determined. The change in total counts will be determined in a measurement where the split detector is rotated above a field.

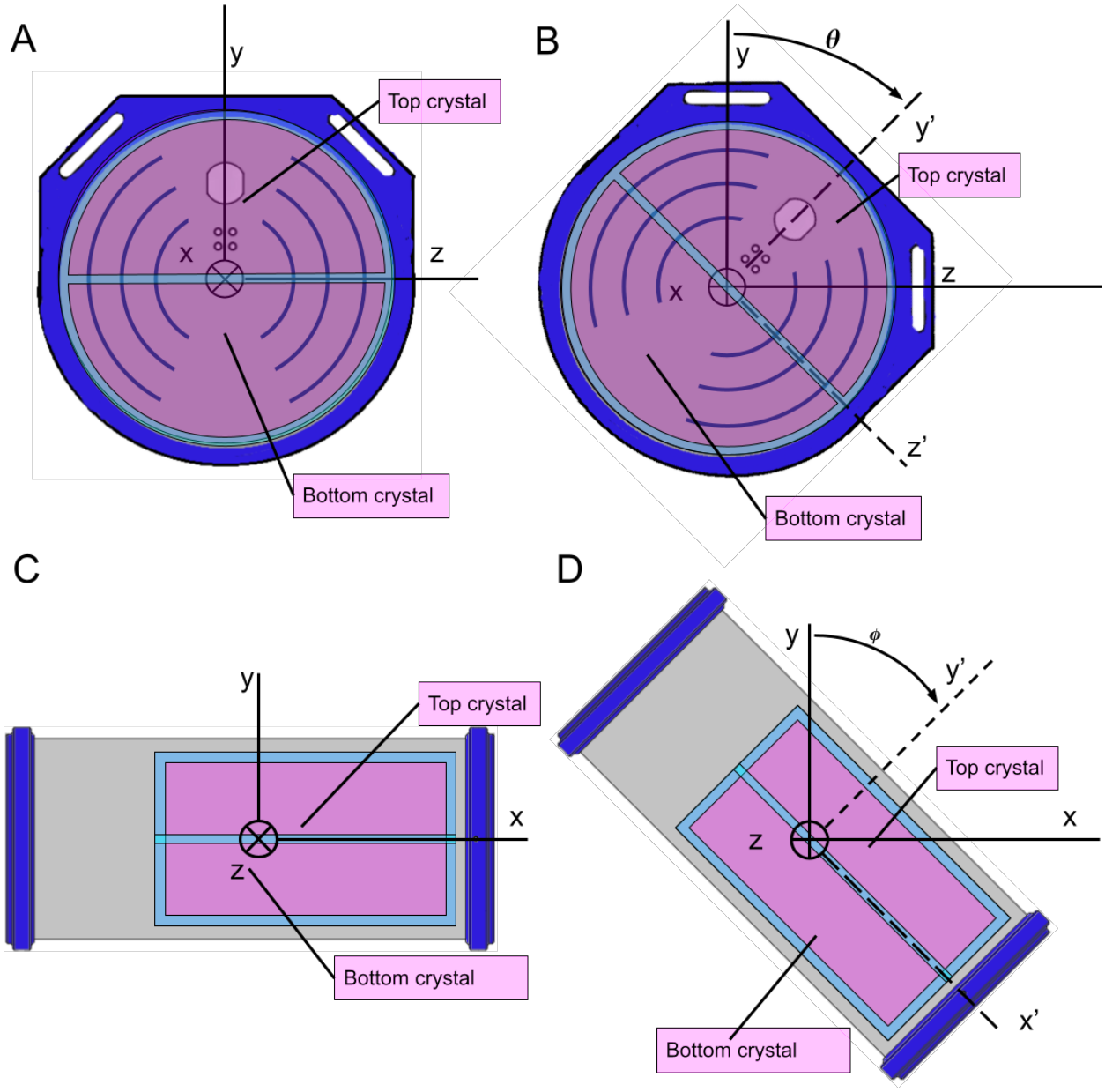

Figure 5.1: Schematic of the split detector from the front and side. The magenta indicates where the scintillation crystals are located inside the detector (not to scale). A: The split detector from the front. B: The split detector from the front, rotated by an angle θ about the x-axis. C: The split detector from the side. D: The split detector from the side, rotated by an angle ϕ about the z-axis.

5.2 Geomtric hypothesis

Under the assumption that the split detector is located above a flat field with homogeneous radionuclide concentrations and a homogeneous radon concentration in the air around the

detector, a maximal difference between top and bottom crystal is expected when the detector is oriented as intended (A and C in Figure 5.1). In this orientation, the bottom (top) crystal maximally shields the top (bottom) crystal from radiation from below (above). After a 90° rotation, no difference in count rate is expected between the crystals, because the plane which separates them is now along the vertical direction.

The summed count rate of both crystals should be the same for all angles, as the total crystal volume and height stay equal in the case of a rotation about the x-axis (see Figure 5.1 B). This summed count rate may change slightly after a rotation about the z-axis. The shape of the combined crystals does not have rotational symmetry in this direction, and the crystals can change height after such a rotation, as in Figure 5.1 D.
The efficiencies are known at certain angles namely, $\eta'_T(\theta = 0°) \equiv \eta'_{T0}$, $\eta'_T(\theta = 90°) = 0.5$, $\eta'_T(\theta = 180°) = 1 - \eta'_{T0}$, $\eta'_T(\theta = 270°) = 0.5$. Where $\eta'_B(\theta) = 1 - \eta'_T(\theta)$. An approximation of $\eta'_T(\theta)$ is thus a periodic function that oscillates around 0.5 with extrema of η'_{T0} and η'_{B0}, a dependence on $\cos(\theta)$ satisfies this and leads to the following equations:

$$\begin{aligned} \eta'_T(\theta) &= 0.5 + (\eta'_{T0} - 0.5)\cos(\theta) \\ \eta'_B(\theta) &= 0.5 + (\eta'_{B0} - 0.5)\cos(\theta) \end{aligned} \tag{5.1}$$

Where this is expected to be the same for every radionuclide except with different values of η'_{T0} and η'_{B0}. This does not take into account Compton scattering, pair-production and the more detailed features geometry of the detector and the source. In Monte-Carlo simulations, these effects can be taken into account, which is described in the next section.

5.3 Simulations

Equation 5.1 shows a hypothesis of how the efficiencies change. This equation is an approximation based on geometry rather than physical arguments, and it does not account for effects such as Compton scattering, pair-production and the geometry of the detector and the source. Monte Carlo simulations incorporate these physical phenomena and were therefore used to check the accuracy of equation 5.1.

5.3.1 Setup

The geometry that was used for the Monte Carlo simulations was a flatbed geometry, as described in Figure 4.5. Simulations were then done with the detector rotated about its x-axis (like in Figure 5.1 A and B) and its z-axis (like in Figure 5.1 C and D) from 0 to 90° in increments of 10°.

For every angle, three simulations were done, one with ^{222}Rn in the first 50 m of air around the detector, one with ^{222}Rn in air except in the first 50 m around the detector, and finally one with ^{238}U in the soil. In the same way as described in 4.3.3. For these simulations Nested DXTRAN spheres, Cell importances, forced capture source biasing and an energy

cut-off for photons of 0.25 MeV, were used to speed up simulations. This can be done because the minimum energy used for radionuclide analysis with the split detector is 0.36 MeV.

5.3.2 Results

Simulations were done where the detector was rotated about its x-axis and z-axis. To calculate the efficiencies, the number of counts per Bq/kg in the 0.25 to 3.0 MeV range due to ^{238}U or ^{222}Rn were determined in each crystal. The number of counts per Bq/kg in each crystal was then divided by the number of counts per Bq/kg in the sum of the crystals.

Rotations about the x-axis

In Figure 5.2 it shows the efficiencies as calculated from simulation and the value predicted equation 5.1. For rotations about the x-axis, the efficiencies calculated by the simulations closely follow the prediction made in the geometric hypothesis.

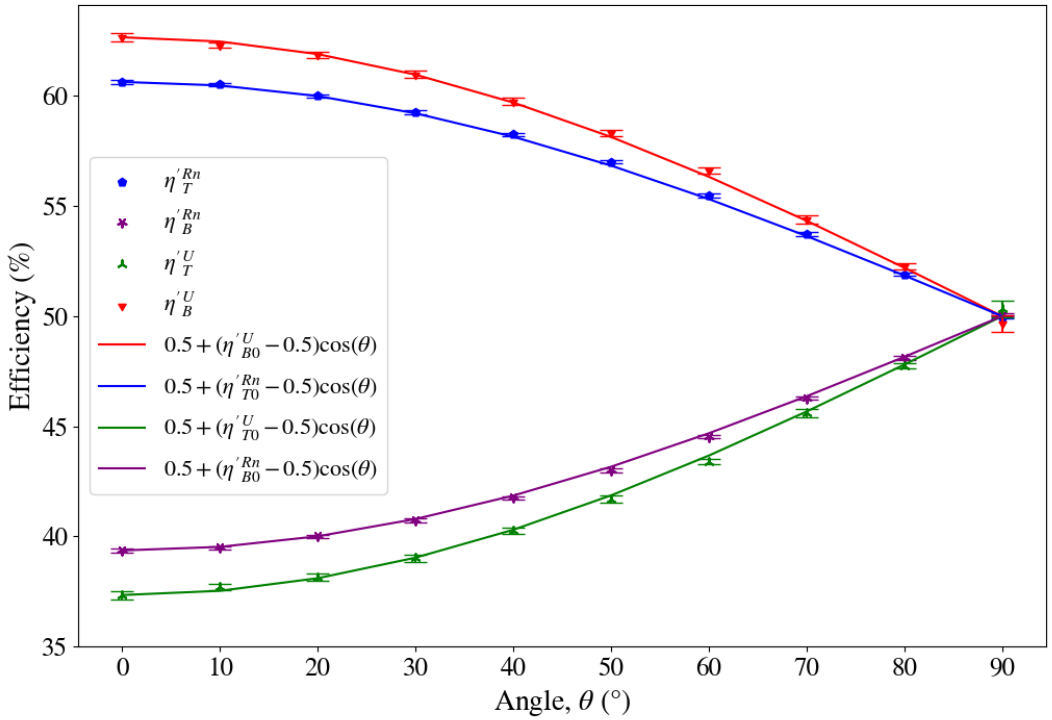

Figure 5.2: The efficiencies determined by the Monte Carlo simulations vs the angle of rotation θ (see Figure 5.1). The points indicate the value from the simulation, and the lines the values that correspond to the geometric hypothesis. Error bars indicate the 1 σ statistical uncertainty from the Monte Carlo simulations.

The simulated values all deviate less than 0.5 percentage points from the predicted values for both ^{222}Rn and ^{238}U. This can be seen in Figure 5.3 which shows the difference between the geometric hypothesis and the outcome of the Monte Carlo simulation. The difference between geometric hypothesis and simulation is within a 1 σ statistical uncertainty for 6 out of 9 points for both radionuclides, which is the expected value if the geometric hypothesis is correct. However, the points in Figure 5.3 do not appear to be distributed randomly around zero. For $\eta_T'^{Rn}$, the geometric hypothesis is slightly less than the result from the Monte Carlo simulation for nearly every angle. Since $\eta_T'^{Rn} + \eta_B'^{Rn} = 1$ that means the opposite is true for $\eta_B'^{Rn}$. For $\eta_B'^{U}$, the difference between simulation and geometric hypothesis is negative for small angles and becomes positive at 30°. From here $\eta_T'^{Rn}$ and $\eta_B'^{U}$ follow a similar pattern with the difference reaching a maximum at 60° before then going back down. For unknown reasons, the uncertainty of the simulation of uranium at 90° was significantly larger than for the rest of the simulations.

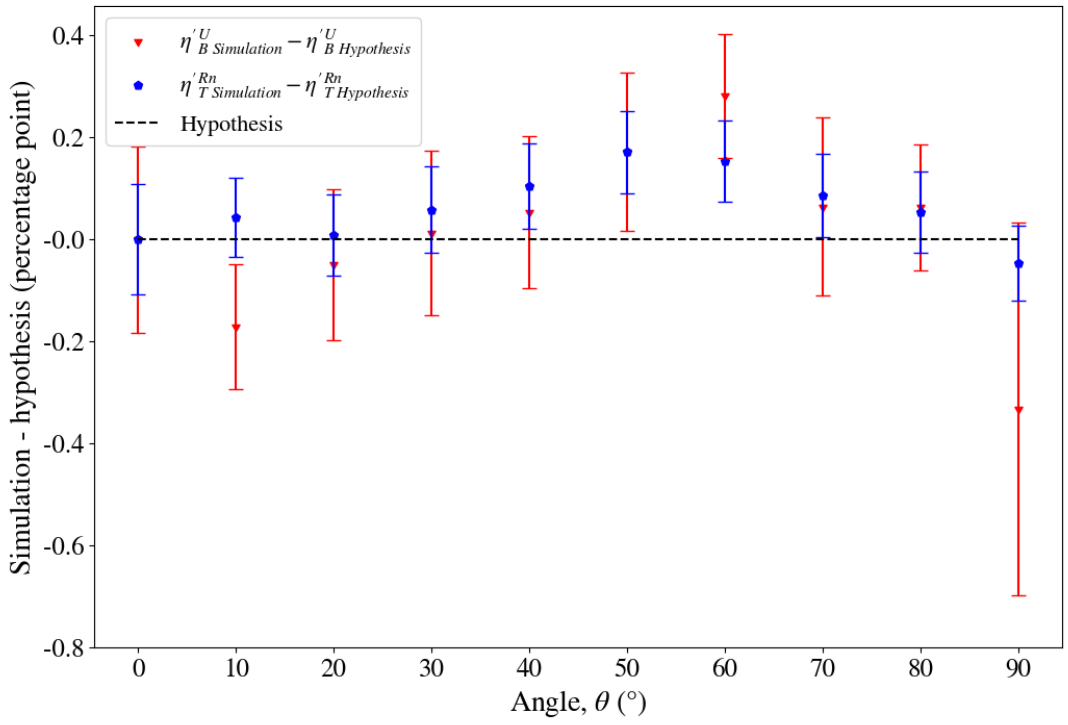

Figure 5.3: The differences between the efficiencies determined by the Monte Carlo simulations and the prediction from the geometric hypothesis vs the angle of rotation θ (see Figure 5.1). The difference is shown for $\eta_T'^{Rn}$ (blue) and $\eta_B'^{U}$ (red) the dashed line indicates the geometric hypothesis. Error bars indicate the 1 σ statistical uncertainty from the Monte Carlo simulations.

Rotations about the z-axis

For rotations about the z-axis, the values of η' at different angles are shown in Figure 5.4. The simulated values all deviate less than 0.6 percentage points from the predicted values for ^{222}Rn and less than 0.03 for ^{238}U. This can be seen in Figure 5.5 which shows the difference between the geometric hypothesis and the outcome of the Monte Carlo simulation.

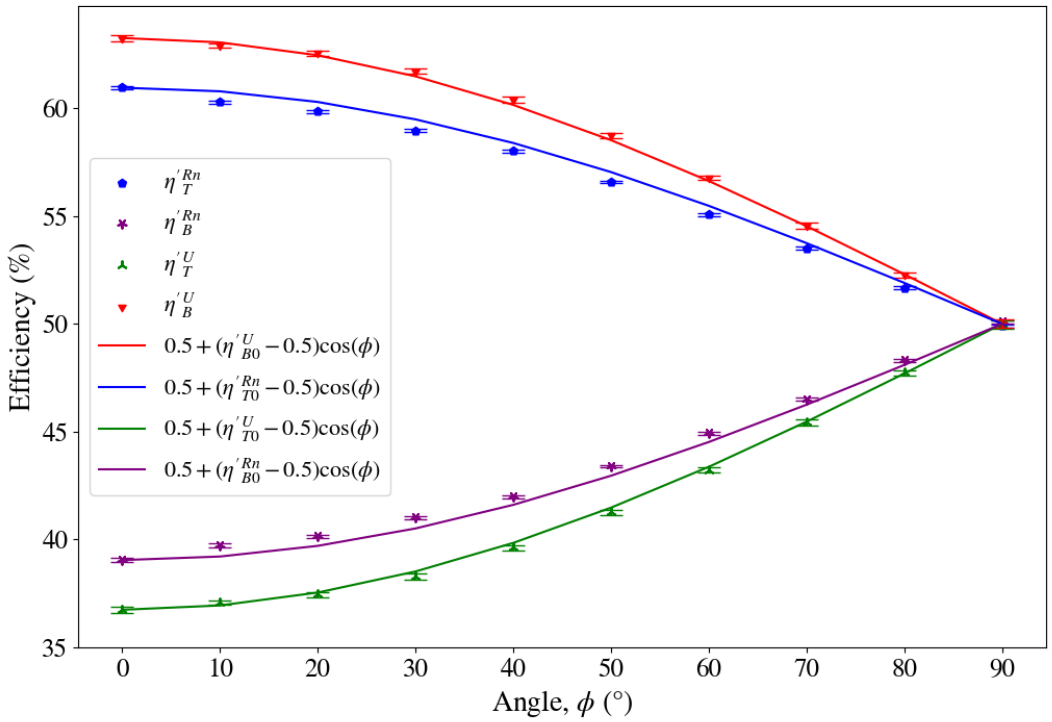

Figure 5.4: The efficiencies determined by the Monte Carlo simulations vs the angle of rotation ϕ (see Figure 5.1). The points indicate the value from the simulation, and the lines the values that correspond to the geometric hypothesis. Error bars indicate the 1 σ statistical uncertainty from the Monte Carlo simulations.

Just as for the rotations about the x-axis, the difference between geometric hypothesis and simulation does not appear to be random. In this case, the geometric hypothesis fall outside the uncertainties for all points with radon. For uranium, the geometric hypothesis is much closer, especially considering that it is based on only 1 simulation. A difference with rotations about the x-axis is that the deviations of the simulation results from the geometric hypothesis followed a somewhat similar pattern for η'^{Rn}_{T} and η'^{U}_{B}, which is not the case for these rotations. The geometric hypothesis is larger than all the results of η'^{Rn}_{T} (Except at 0° which is zero by design) whereas the geometric hypothesis is mostly smaller for η'^{U}_{B}. In the case of $\eta'^{Rn}_{T(B)}$, there is a notable difference between the value at 0° and 10° which is 0.5 percentage points

larger than expected, this difference then persists for larger angles until it starts to decrease at about 60°.

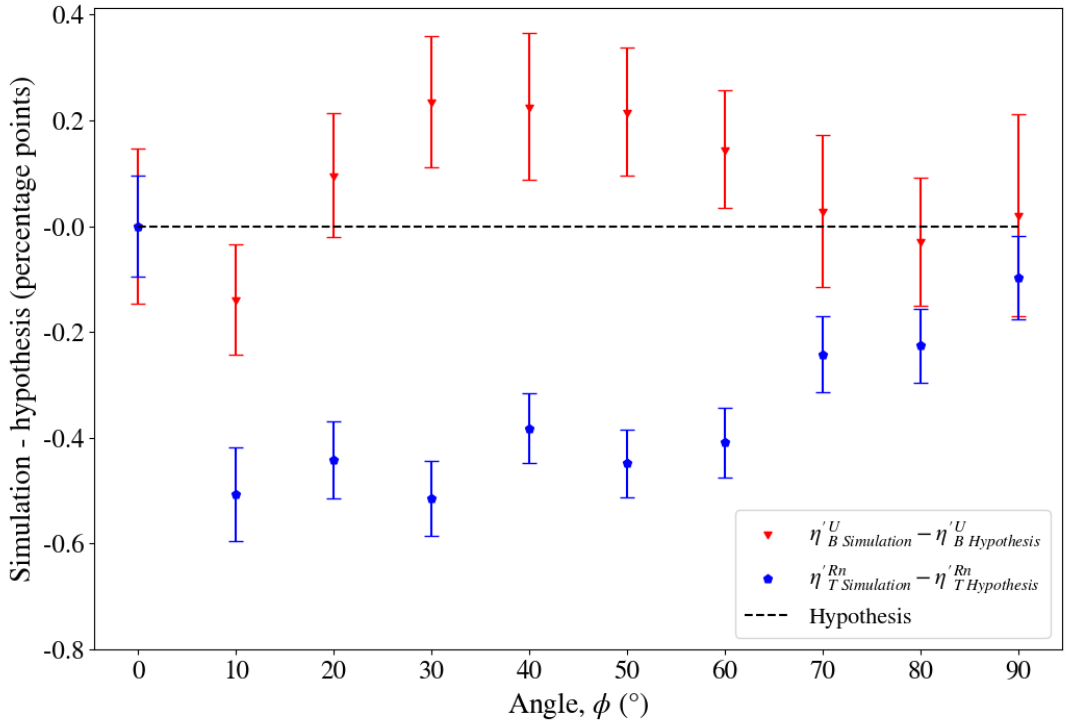

Figure 5.5: The differences between the efficiencies determined by the Monte Carlo simulations and the prediction from the geometric hypothesis vs the angle of rotation ϕ (see Figure 5.1). The difference is shown for η'^{Rn}_{T} (blue) and η'^{U}_{B} (red). The dashed line indicates the geometric hypothesis. Error bars indicate the 1 σ statistical uncertainty from the Monte Carlo simulations.

5.4 Field measurement

To determine the impact of rotating the split detector during a geophysical survey, measurements were done in a field where the detector was rotated over various angles. A single measurement at every angle was made for 5 minutes. The total number of counts (γ-rays) that were detected during the measurement in each crystal was divided by the live time, which is the actual time when the detector is registering counts. For these measurements, only the total counts per second are considered, as this does not require any spectrum analysis. By dividing by the total number of summed counts of both the crystals at each angle, changes in temperature and crystal height in case of the rotations about the z-axis, which can affect the total counts, are cancelled because we assume the temperature and change in average crystal height to be the same for both crystals. This also allows for

a comparison between measurement and geometric hypothesis, because the geometric hypothesis predicts how the distribution of radiation in the crystals change with rotations in the case that γ-rays originate preferentially from one direction. In this case, more γ-rays are expected to come from below.

5.4.1 Setup

An experimental setup was built, which allowed the detector to be easily rotated 360° about its x-axis and 180° about its z-axis at a height of about 80 cm. This setup can be seen in Figure 5.6. It consisted of a metal post on a metal plate that was held straight with some ropes and pegs.

A wooden board was attached to this metal post at two points. In the wooden board, nineteen 1 cm holes were cut using a laser cutter in a semicircle spaced 10° apart, with a hole in the centre of the semicircle as well. Through these holes, the wooden board was bolted to the clamps that were holding the metal post. The holes in the centre could be used with any of the holes on the semicircle to be able to rotate the board 180°.

A shelf was attached to this wooden board at a 90° angle, fortified with shelf brackets, and with holes allowing the detector to be securely attached. If the wooden backboard was rotated to some angle, the shelf and the detector attached to it, would rotate accordingly. This made it possible to rotate the detector about its z-axis at any angle between -90° and 90° that is a multiple of 10°.

In order to rotate the detector about its x-axis, a plexiglass construction was made with a semicircle cut out, that had the same diameter as the carbon fibre tube of the split detector. In this construction, the split detector could lie stable at any angle. On the plexiglass, markings were made every 10° to track the angle of the detector by aligning them with the screws that attach the end cap of the detector to the carbon fibre tube. The plexiglass construction, with the detector on it, was placed on the wooden shelf when it was horizontal. The detector could then be rotated about its x-axis.

Figure 5.6: Photographs of the experimental setup that was used to measure with the split detector at various angles. The side where the cable comes out of the detector is the front. The crystals are positioned to the back of the detector (as illustrated in Figure 4.1).

For this experimental setup, it was estimated that there was an uncertainty of 2° for both rotations about the z- and x-axis. This uncertainty comes from any instability in the metal post holding the wooden construction. There was also some wiggle room in the way the wooden board was bolted to the clamps holding the metal post. This was likely a small effect. There may have been some slight misalignment of the detector with the markings on the plexiglass because this was done by eye.

Next to the split detector and a rotation setup, another necessary requirement was to have a field. The field that was chosen to perform this measurement was located in Groningen at approximately 53.2102° N, 6.6157° E. The measurement was conducted between 2 and 5 pm on March 3rd 2023 under dry weather conditions. The main requirements for this location were that the ground was flat, that it was not surrounded by buildings and trees. The 99 % footprint of a γ-ray detector at 0.8 m is about 67 m[11]. within this range there were some trees and water. The assumption was made that these did not interfere with the measurement.

Ideally, the field used for this measurement should have homogeneously distributed radionuclide concentrations. If large variations exist within this field, this can cause differences between horizontally looking crystals. No test was done to assess the homogeneity of the field. However, if on one side of the detector the soil is radionuclide rich and on the other the soil is radionuclide poor, the difference should be still be much smaller than the difference between ground and air. The effect of inhomogeneity will become more pronounced, for rotations close to 90°.

5.4.2 Results

Rotations about the x-axis

In Figure 5.7, the response of the split detector is shown when at various angles of rotation about the x-axis. In this case, the angle 0° means that crystal 1 was looking straight down to the ground. In this orientation, crystal 1 received about 58 % of the radiation. As the split detector was rotated, crystal 1 detected less radiation and crystal 2 more. According to the geometric hypothesis, this should follow a cosine shape. In Figure 5.7 a cosine is drawn based purely on the detector at an angle of 0° in line with the geometric hypothesis. The shape of the cosine appears to closely follow the data points for the entire 180° range that was measured.

Rotations about the z-axis

The split detector was used to measure at different angles of rotation about its z-axis. Measurements were taken from -80° to 90° with 0° being the detector oriented horizontally with crystal 1 looking down. In Figure 5.6 the detector is shown at an angle of 90° in the top right and 40° in the bottom left. Because of the way the setup was designed, both crystals were closer to the ground at positive angles and further from the ground at negative angles.

Figure 5.7 shows the response of the split detector at various angles of rotation about the z-axis. For rotations about the z-axis, more points are further removed from the geometric hypothesis than for the rotations about the x-axis, however, the prediction is still within a percentage point of the result.

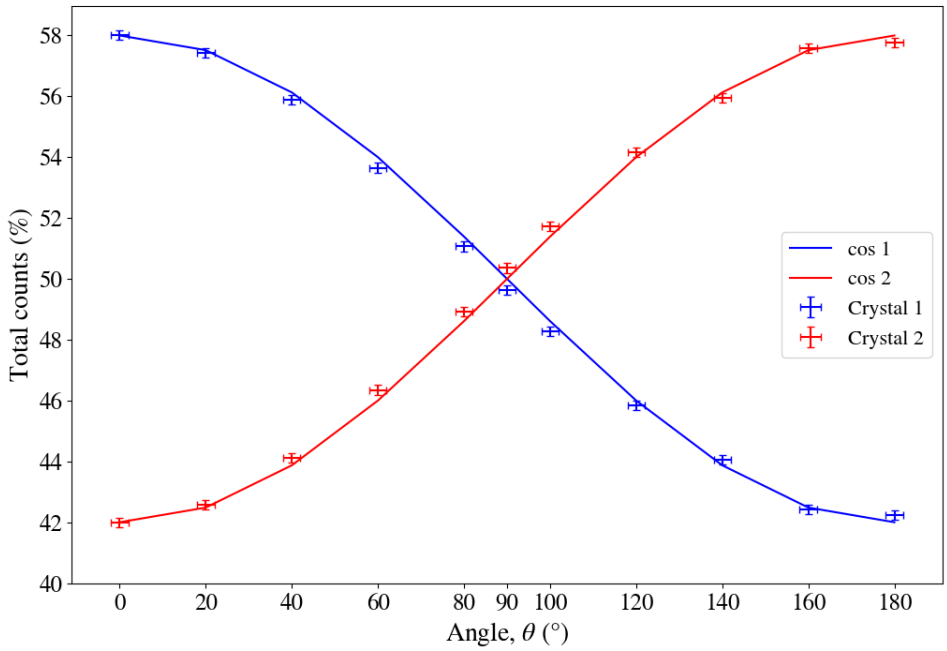

Figure 5.7: The distribution of the total counts vs the angle of rotation about the x-axis of the detector. On the x-axis the angle of rotation, and on the y-axis the number of total counts in crystal 1 (blue) and crystal 2 (red) divided by the number of total counts in both crystals. the number of total counts was scaled for both crystals using the overall scaling factor that was determined in the calibration. A cosine is also drawn in line with the geometric hypothesis, with η_{T0} being determined from the measurement at an angle of 0°.

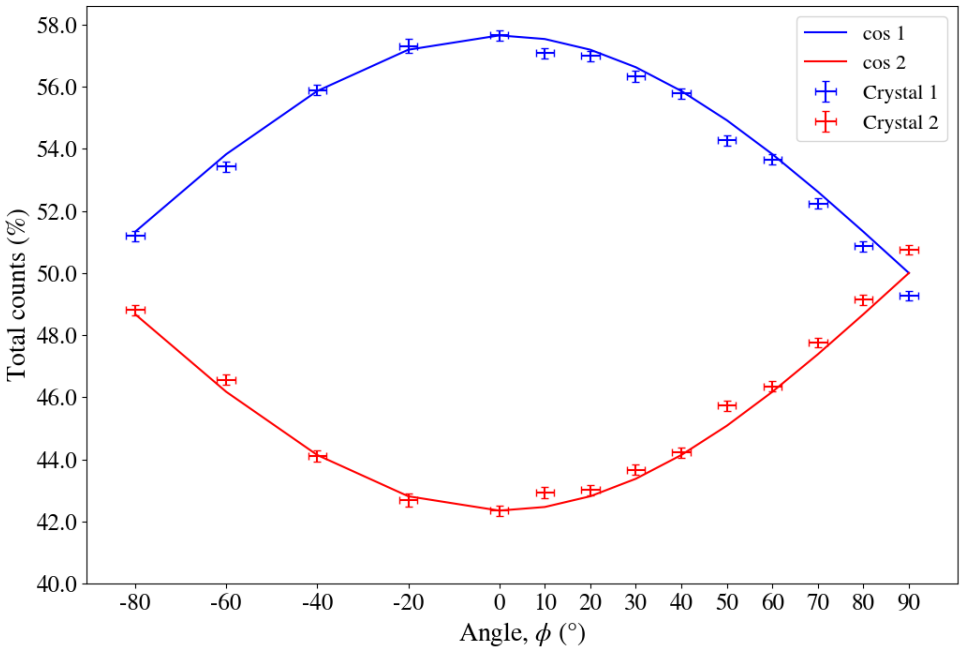

Figure 5.8: The distribution of the total counts vs the angle of rotation about the z-axis of the detector. On the z-axis the angle of rotation, and on the y-axis the number of total counts in crystal 1 (blue) and crystal 2 (red) divided by the number of total counts in both crystals. the number of total counts was scaled for both crystals using the overall scaling factor that was determined in the calibration. A cosine is also drawn in line with the geometric hypothesis, with η_{T0} being determined from the measurement at an angle of 0°.

5.5 Discussion and conclusion

When the split detector is rotated, its response is influenced. The change in response can be approximated by a cosine of the angle, this was confirmed by both simulations and measurements. Not only is the rate of change in η' slower at smaller angles due to a cosine dependence, for equation 3.4 this holds as well. while at 90°, equation 3.4 diverges. Because the change in response can be approximated by a cosine function, angular fluctuations of less than 20° around 0° can be neglected. The change, caused by this amount of rotation, will be smaller than 10 %, which are typical statistical uncertainties of the radionuclide concentrations calculated from the spectra.

If the detector is used in a rotated orientation during a measurement, this can be considered in the analysis of the measurement. An example of this could be a drone which is pitched forward for the entire flight duration. In such a situation, the user of the split detector should keep track of the orientation of the detector during the measurement, which can be done if a UAV is used to perform the measurement which measures its own

orientation. The orientation alongside a timestamp can be saved during a flight, these flight angle measurements can be synchronised with the γ-spectrum measurements so that a correction can be applied. In the analysis of such a measurement, one can either try to match the angle to Monte Carlo simulations of the split detector in the same angle, or apply a correction based on equation 5.1. To apply a correction based on equation 5.1, calculate the values of η' using equation 5.1 using the known values of η_0 and the angle, then use equation 3.4 to calculate the ^{222}Rn and ^{238}U concentrations, using the adjusted values of η'. Corrections can not be applied at 90°, at divide by 0 errors will appear in due to all η' being zero.

More research can be done into the effect of rotations on the response of the split detector by doing a full radionuclide analysis at several angles and seeing how the measured concentration of each nuclide responds to rotations. Corrections may be applied to this measurement to see if applying the correction produces the same result regardless of rotation.

Chapter 6

Radon measurement with the split detector

6.1 Introduction

The split detector was designed for the purpose of correcting for the presence of atmospheric radon during a geophysical survey. With the detector having been calibrated, it was ready to be deployed to see if it is capable of correcting for radon. In order to test this, the split detector was deployed in a stationary measurement. During this measurement, the radon concentration was monitored next to it using an independent and well validated method in order to answer:

- **Does the split detector correct for the presence of ^{222}Rn?**
- **Is the split detector capable of determining the ^{222}Rn concentration?**

In this chapter, the experiment that was done to answer these questions is described in detail. First, the location and setup of the experiment will be described. Then, the results of the measurement will be presented and discussed, and finally these questions will be answered in the conclusion.

6.2 Lutjewad

In order to test if the split detector is able to accurately determine the concentration of atmospheric radon and soil uranium. It was necessary to do a measurement with the split detector next to a different method of determining the atmospheric radon concentration. The location that was chosen to perform the measurement was the Lutjewad atmospheric measurement station.

The Lutjewad atmospheric measurement station, is owned and operated by The Center for Isotope Research of the University of Groningen[57]. It is located just behind the Wadden

Sea dyke near Hornhuizen in Groningen, The Netherlands.

The measurement station comprises a tall mast standing at 60 meters, accompanied by a small laboratory building adjacent to it. The mast houses advanced equipment dedicated to studying the greenhouse effect, featuring air inlets positioned at heights of 7, 40, and 60 meters. These inlets facilitate the pumping of air into the laboratory. Various measurements are conducted on-site, and automated systems ensure that glass bottles are filled to be taken to Groningen for further analysis. At Lutjewad measurements are done of greenhouse gasses such as CO_2, CH_4 and NO_2 as well as tracers such as carbon isotopes, COS and ^{222}Rn[58].

Atmospheric concentrations of ^{222}Rn are monitored using an ANSTO dual-flow loop two-filter detector, as described by Whittlestone and Zahorowski in 1998[59]. The measurements are taken at half-hourly intervals. The time it takes for air to travel from the air inlet at 60 m height to the detector located in the laboratory is about 10 minutes. The detector measures α-particles and is not energy selective, making it sensitive to both ambient ^{220}Rn (with a half-life of 55.6 seconds) and ^{222}Rn. ^{220}Rn is filtered out because it takes air roughly 10 half-lives for air to reach the detector. To remove aerosols and radioactive decay products, a filter is placed in front of the detector. The decay products of ^{222}Rn are then sampled on a second filter inside a 1500 litre delay chamber, where their decays are counted using a scintillator and a photomultiplier. The measurement uncertainty of the system depends on the total counts and the uncertainty of the ^{222}Rn source used to calibrate the device. The uncertainty is typically around 5 %[60].

6.3 Experimental setup

The goal of the experiment was to measure the outdoor radon concentration with the split detector and see if it could be used as a viable way to correct for its presence. To do this, it is beneficial to measure at various outdoor radon concentrations such that a correlation can be made with the radon concentrations that are measured by the detector from Lutjewad and the split detector.

Prior to the experiment, the data from radon measurements done at Lutjewad from January 2006 to January 2023 was assessed. The radon concentration at Lutjewad in this period averaged 1.78 Bq/m^3 and had a median of 1.16 Bq/m^3 [24]. This is on the low end compared to other geographical locations where averages have been reported up to 23 Bq/m^3[25][26]. In theory, the split detector is able to reach a smaller statistical uncertainty on the radon concentration if the radon concentration is larger. During the experiment, variations in radon concentrations are desired. The radon concentration at Lutjewad is mostly low, and peaks in radon concentration do not happen on a daily or even weekly basis. Atmospheric radon concentrations are unpredictable, so it is not known when a peak

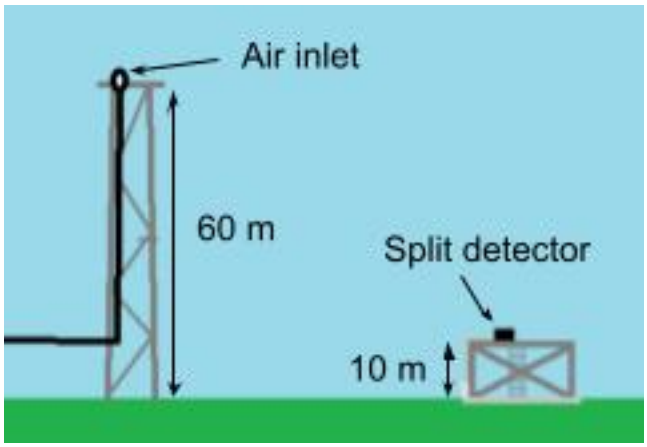

Figure 6.1: A schematic picture of the measurement setup at Lutjewad. With on the left, the 60 m Lutjewad mast with the air inlet that sucks in air for radon detection, and on the right the scaffolding on which the split detector was placed.

will happen. During a period of a month, it seemed likely enough that a peak of up to at least 5 Bq/m^3 would occur. For that reason, the split detector was deployed for at least a month at Lutjewad during which it measured continuously.

Next to the 60 m mast, a 10 m high scaffolding is located, on top of which the detector was placed. This is illustrated in Figure 6.1. Although the detector is meant to be weather resistant, it would be outside for a long period of time. As a precaution to ensure that the detector survives all weather conditions during the measurement, it was placed in a waterproof plastic case. Power and Ethernet cables were pulled through waterproof cable glands in the side of the case to power the detector and be able to connect to it remotely. Foam was used to keep the detector in place.

The measurement geometry differs from the Monte Carlo simulations, where the detector was free floating at 10 m above a perfectly flat soil with homogeneous sources of radionuclides. The radionuclide distribution in the soil below it is unknown, on top of the scaffolding, two measurement apparatuses are placed, and the scaffolding is placed next to a sea dyke. These are shown in Figure 6.3. It was not researched how large of an impact these geometry changes make, and for the spectrum analysis that was done the flatbed Monte Carlo simulations described in 4.3.3 were used.

While a comprehensive investigation was not conducted to evaluate the impact of the geometry differences, an estimation was made to assess their potential effects. The scaffolding is expected to have a small impact since it is non-radioactive and thin, primarily serving as a shield for radiation from below. The measurement apparatuses shield radiation from a small solid angle, indicating they would likely have a minor influence on the measurements. The sea dyke, being a substantial structure, is anticipated to block almost all radiation travelling through it. With approximately 50 m of distance

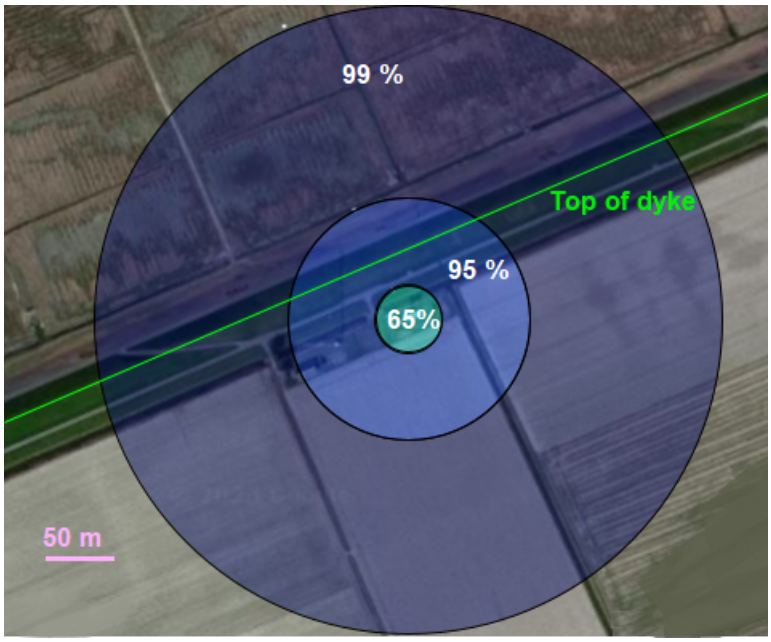

Figure 6.2: The footprint of the Lutjewad measurement. With the concentric circles indicating the which area of land would contribute 65, 95 and 99 % of the radiation from the ground if it were flat.[61]

between the top of the dyke and the detector, most of the detector's footprint remains unaffected (see6.2). Additionally, since the detector is positioned higher than the top of the sea dyke, it does not obstruct horizontally travelling radiation. As the dyke is made of earth, it contains radionuclides, which will contribute to the measured spectra.

The split detector was installed on the Lutjewad scaffold on March 15^{th} 2023, with crystal 1 facing up. The detector measured in this orientation until May 12^{th} 2023. On that day, the detector was flipped, with crystal 2 facing up. The detector was flipped to see if it would change the results. If there is an issue with the calibration, flipping the detector could impact the results. This measurement is still ongoing at the moment of writing this report. During this time, the detector continuously measured γ-ray spectra and PTH data (Pressure, Temperature and Humidity). The detector output was set at 1 Hz.

6.3.1 Data processing

To ensure a consistent temporal spacing between data points and to minimize the data volume for computational efficiency. The 1-second raw spectra were summed up on a minute-by-minute basis, operating under the assumption that the temperature variations within this timeframe would be minimal, as temperature changes can impact the raw spectra. For PTH data, this involved calculating the average value per minute.

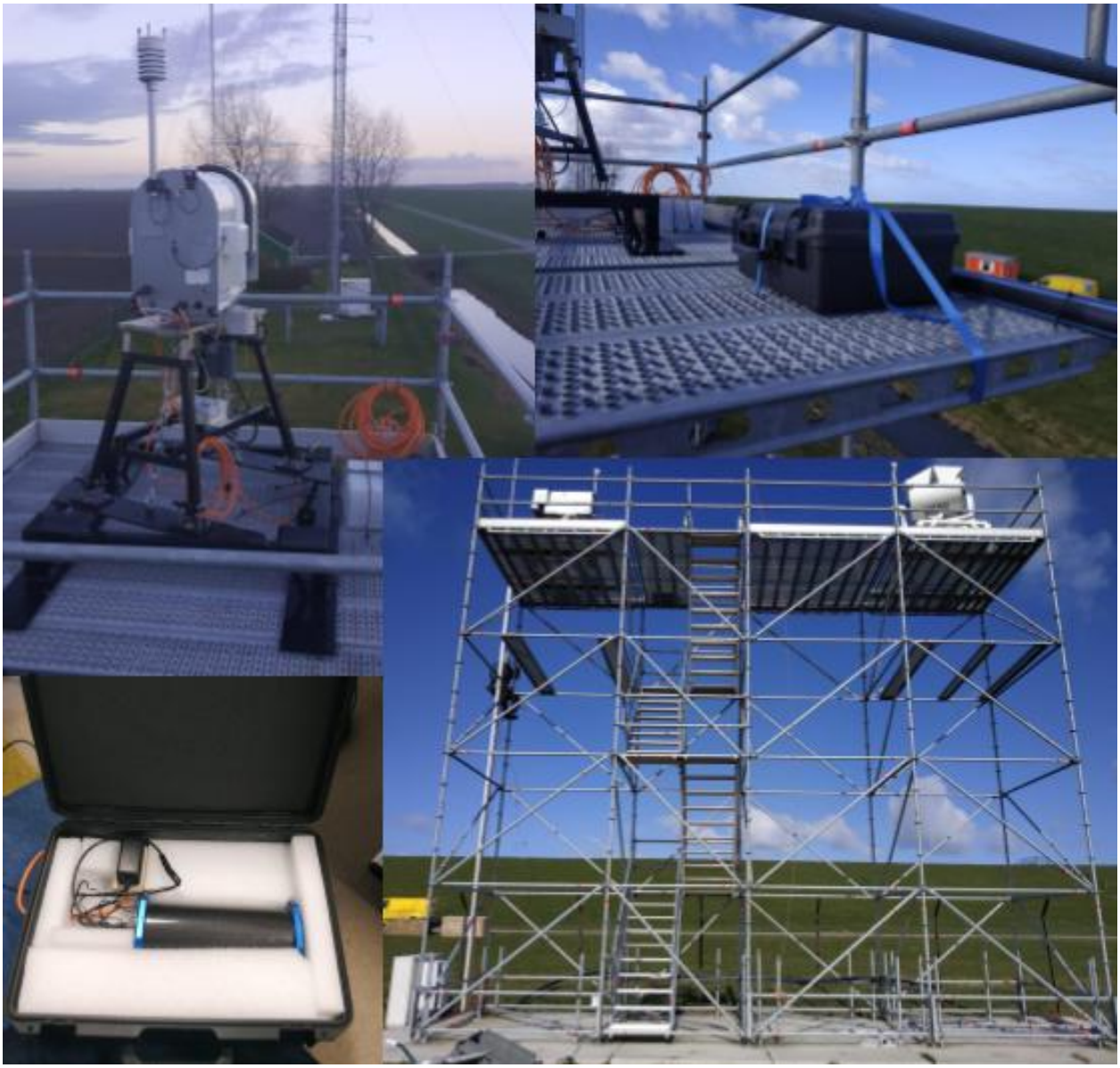

Figure 6.3: Pictures of elements of the measurement setup in Lutjewad. With on the top left a picture taken from the top of the scaffolding with a measurement apparatus on top of the scaffold and the 60 m mast and Lutjewad laboratory building in the background. In the top right picture, the case within which the split detector is located secured to the scaffold. In the bottom left, the split detector is seen inside the opened case, this picture was taken inside the Medusa office. In the bottom right, a picture of the entire scaffold structure with in the background the Wadden Sea dyke.

The 1-minute PTH and spectrum data for each crystal was combined with the corresponding calibration file and loaded into GAMMAN. GAMMAN is a software toolkit, developed by Medusa Radiometrics BV, designed for the automated analysis of γ-spectra gathered during geophysical surveys. In order to synchronise with ^{222}Rn measurements of Lutjewad, the 1-minute data was integrated into 30-minute intervals using GAMMAN, which stabilises for temperature fluctuations within that period. GAMMAN conducted a full spectral analysis for each 30-minute segment, enabling the determination of radionuclide concentrations at 30-minute intervals.

For unknown reasons, there is no split detector data (PTH and spectrum) from 10:00 pm, March 17th to 9:45 am, March 18th. The uptime of the detector indicated that the system had been running continuously since the start of the experiment, so the detector was not turned off during that time. At a few moments[1] throughout the measurement, there is either no PTH, or no spectrum data. Missing spectrum data is no problem, because each spectrum is associated with a live time. Live time is used in the spectrum analysis, which means this is automatically corrected for. The result is simply larger statistical uncertainty when this occurs. Missing PTH data is a problem because this causes wrong temperatures to be associated with spectra[2], which causes wrong temperature corrections to be applied to the measured spectra. Therefore, spectrum data without associated PTH data was not used in the analysis.

6.4 Results

The count rate measured by both detector crystals over time is shown in Figure 6.4, it is also shown when it rains. The rain data that was used was taken from a weather station from the KNMI located at Lauwersoog 12 km west of Lutjewad[62]. During the entire measurement, the bottom crystal measured more counts per second than the top crystal. At some points in time, large peaks can be seen in the count rate for both crystals. These peaks in count rate appear to be coincident with rainfall.

The radionuclide concentrations that were determined by each crystal can be seen in Figure 6.5, again with rain data in the same figure. The calculated ^{238}U concentrations include ^{222}Rn contributions, no correction has been applied yet. The concentration of ^{238}U has peaks in the same way as the count rate during moments of rain, showing increases in concentration of up to a factor. For ^{232}Th the measured concentration for the top crystal remained between 25.4 ± 0.4 and 29.6 ± 0.5 Bq/kg during dry periods. With rain, the measured concentration drops, with a minimum of 22.0 ± 0.4 Bq/kg. For the bottom crystal the values fluctuated less with concentrations between 25.1 ± 0.4 and 28.9 ± 0.5 Bq/kg in dry periods. Concentrations

[1] With the 12-hour period of March 17th to March 18th excluded, this happens 10 times during the measurement, with dead times ranging from 5 to 220 seconds

[2] Due to the way the output of the detector was processed, the temperature would always be 0°C when this happens.

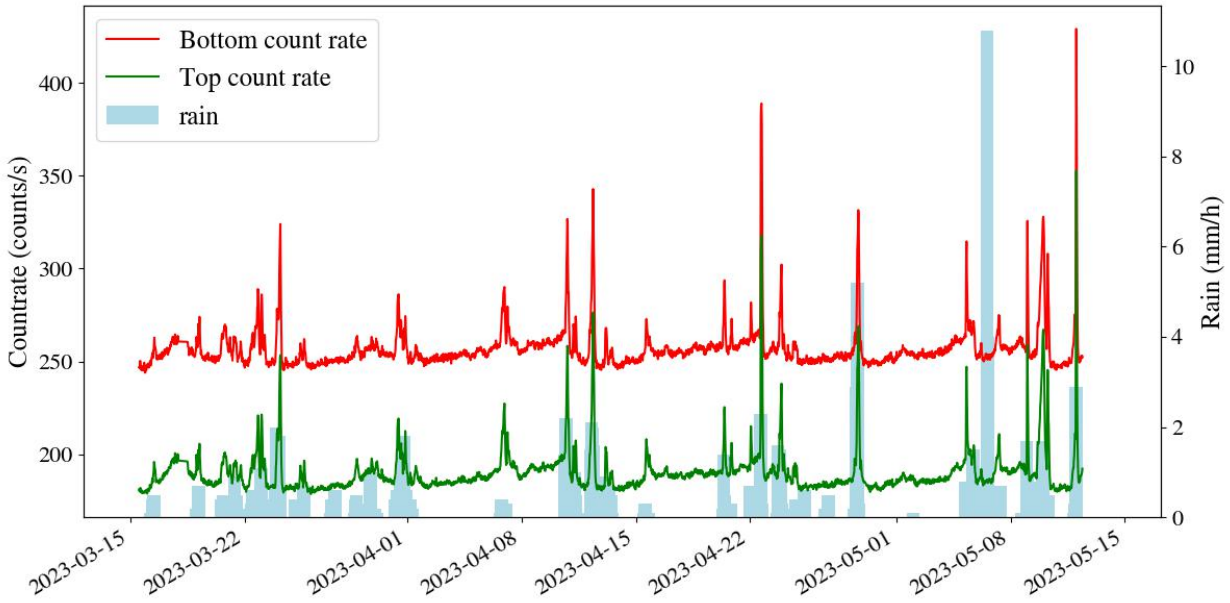

Figure 6.4: The timeline of the rain and count rate. With light blue bars indicating the rainfall in mm/h on the left y-axis, and the count rate is shown on the left y-axis in counts per second.

were also less sensitive to rain in the bottom crystal, a minimum of 23.1 ± 0.4 Bq/kg was observed. For ^{40}K, a similar pattern was observed for the top crystal, except now with a range of 235 ± 4 to 276 ± 4 Bq/kg and a minimum of 208 ± 5 Bq/kg during rain. For the bottom crystal, concentrations in dry periods were observed between 249 ± 4 and 285 ± 4, with a minimum of 250 ± 4 Bq/kg during rain.

Figure 6.6 displays the relationship between radionuclide concentrations and the count rate measured in each crystal. In both crystals, the count rate is positively correlated to the ^{238}U concentration. The top and bottom crystal have a Pearson correlation coefficient of 0.98 and 0.97 respectively.

Figure 6.7 shows the ^{238}U and ^{222}Rn concentrations calculated from the uranium spectra using equation 3.4 next to the ^{222}Rn concentration measured by Lutjewad. Peaks in the ^{238}U concentration still happen, but only during times of rain. The ^{222}Rn concentration measured by Lutjewad is lower than that measured by the split detector.

Rain

During rain, peaks in count rate are observed. These peaks are attributed to an increase in ^{238}U in both crystals of the split detector. The ^{222}Rn measurements from Lutjewad do not indicate an increase in ^{222}Rn of the same magnitude during times when this happens. A possible explanation for this, is that ^{222}Rn daughters in the atmosphere bind to aerosols

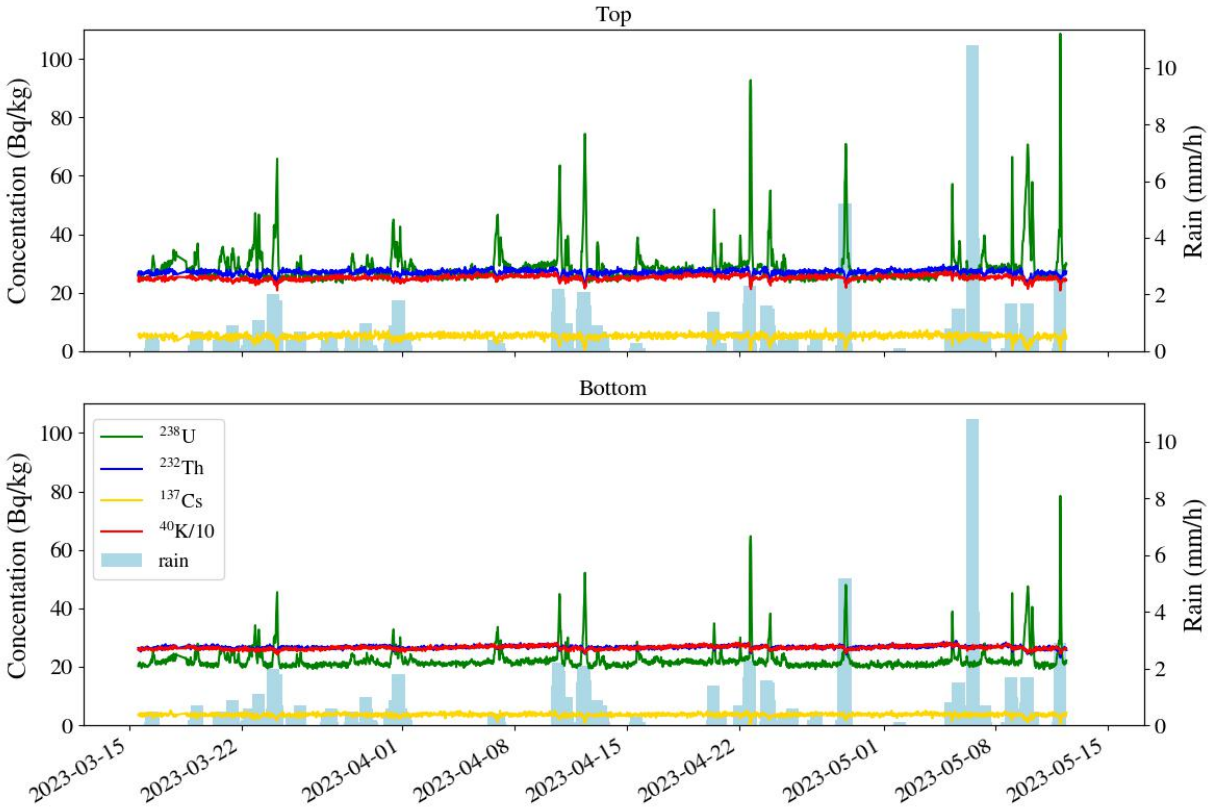

Figure 6.5: The radionuclide concentrations calculated by each crystal and rain during the measurement. With light blue bars indicating the rainfall in mm/h on the left y-axis, and the concentrations of the radionuclides ^{137}Cs, ^{232}Th, ^{238}U and the concentration of ^{40}K divided by 10 are shown on the left y-axis in counts per second.

which fall to the ground when it rains[19]. These daughters (^{214}Pb and ^{214}Bi) are the most prominent γ-ray emitters in the ^{238}U decay chain. After rain, these daughters are suddenly much closer to the detector, which explains why an increase in ^{238}U and ^{222}Rn is observed. The ^{222}Rn detector from Lutjewad filters aerosols before measurement. As a result, these peaks are not observed in their ^{222}Rn measurement.

Split detector measurements during and shortly after rain are not an accurate representation of the soil ^{238}U concentration and air ^{222}Rn concentration. The soil now has increased concentrations of ^{214}Pb ($T_{1/2}$ = 27.1 minutes), ^{214}Bi ($T_{1/2}$ = 19.7 minutes), and the air is out of equilibrium. After 3 hours, the increased activity at ground level due to these radionuclides should have reduced to about 1% and secular equilibrium should be restored. For the rest of the analysis, the measurements during, and 3 hours after rain are disregarded.

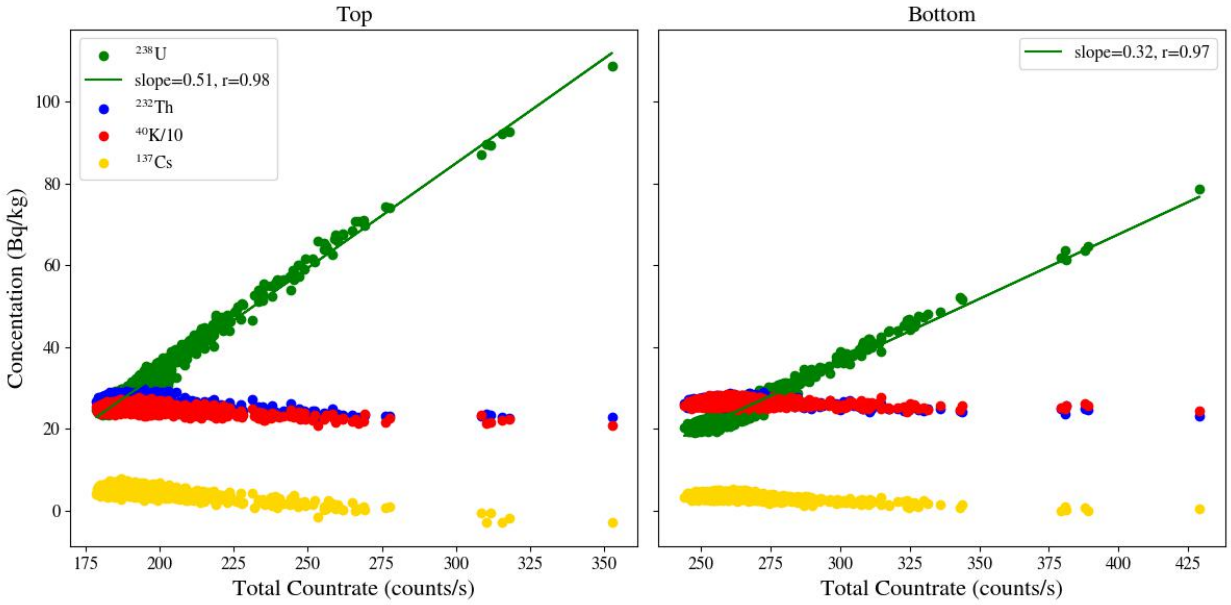

Figure 6.6: The radionuclide concentrations vs the count rate for the top and bottom crystals. With the radionuclide concentrations (^{40}K is divided by 10) on the y-axis and the count rate on the x-axis.

Dry results

In Figure 6.8, the detected concentration of ^{238}U in the top crystal, bottom crystal, and the concentration determined by equation 3.4 are plotted against the measured ^{222}Rn concentration by Lutjewad. Additionally, the measured ^{222}Rn concentrations are plotted against those of Lutjewad. The parameters of the linear fit and correlation coefficients are shown in Table 6.1.

The ^{238}U concentration for each individual crystal exhibits a positive correlation with the ^{222}Rn concentration in the air. Upon applying Equation 3.4, the ^{238}U concentration shows a correlation coefficient of $r = -0.1$.

The ^{222}Rn concentration measured by the split detector exhibits a higher value compared to the measurement obtained by Lutjewad. The two ^{222}Rn measurements display a positive correlation, with a correlation coefficient of $r = 0.64$. To enhance the correlation between the two, a Savitzky-Golay filter [63] can be applied. By fitting a polynomial of order n through m data points, the Savitzky-Golay filter reduces the noise, resulting in smoother more gradual changes over time. The ^{222}Rn data collected from the split detector is susceptible to noise, this noise is reduced by employing the Savitzky-Golay filter.

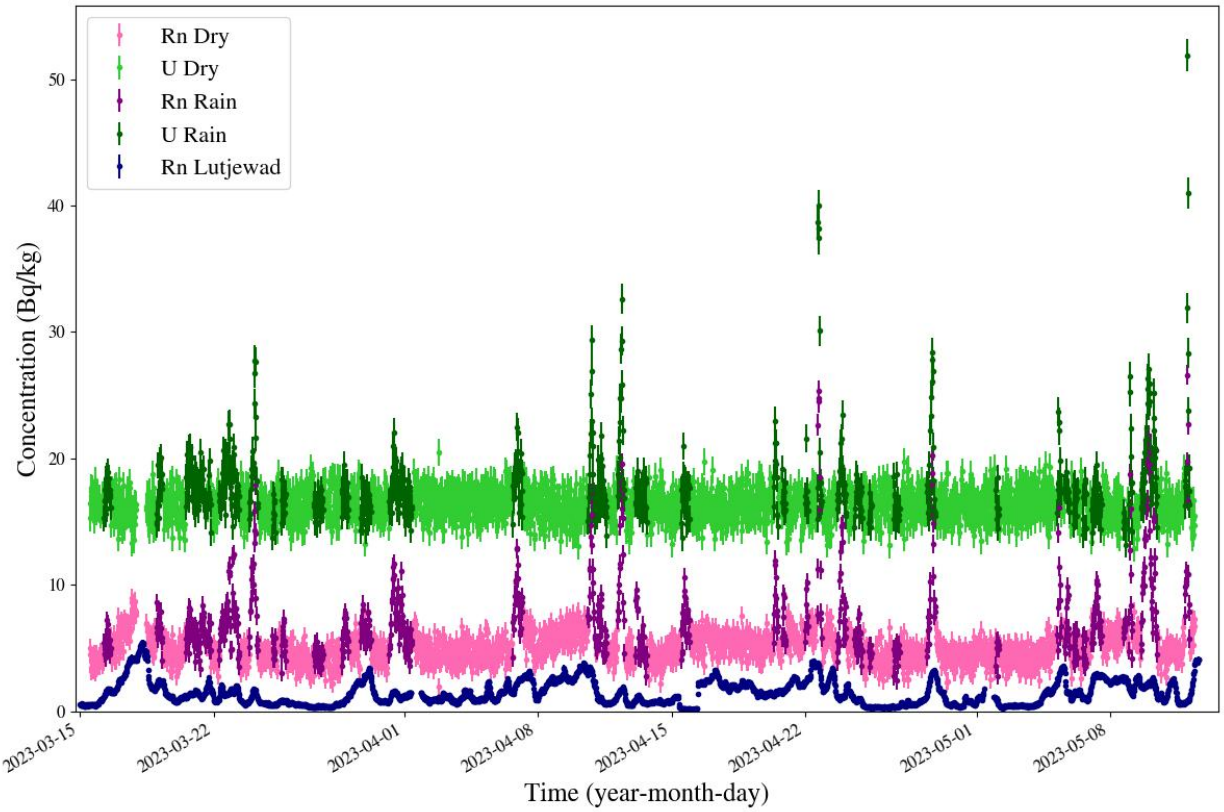

Figure 6.7: ^{238}U and ^{222}Rn concentrations, measured by the split detector, and ^{222}Rn concentration measured by Lutjewad over time. The light green and pink points are ^{238}U and ^{222}Rn measured by the split detector during dry periods. The dark green and purple points are ^{238}U and ^{222}Rn measured by the split detector during and 3 hours after rain.

	Slope	Intercept	r
^{222}Rn	0.78	3.85	0.64
^{222}Rn Smoothed	0.73	3.91	0.88
^{228}U corrected	-0.13	16.48	-0.1
^{228}U Top	1.52	24.68	0.8
^{228}U Bottom	0.64	20.32	0.66

Table 6.1: The parameters of the linear fit of the data shown in Figure 6.8

By limiting the window size to one day ($m = 48$) and the polynomial order to $n = 4$, the highest correlation coefficient is achieved when $m = 19$ and $n = 1$. This was determined by testing every combination within the limits and choosing the one with the highest correlation coefficient. This implies that a polynomial of order 1 is fitted through the 19 values[3]. After applying the Savitzky-Golay filter with $m = 19$ and $n = 1$, the correlation

[3]Each point contains 30 minutes of data. A straight line is therefore fitted through 9 hours and 30 minutes

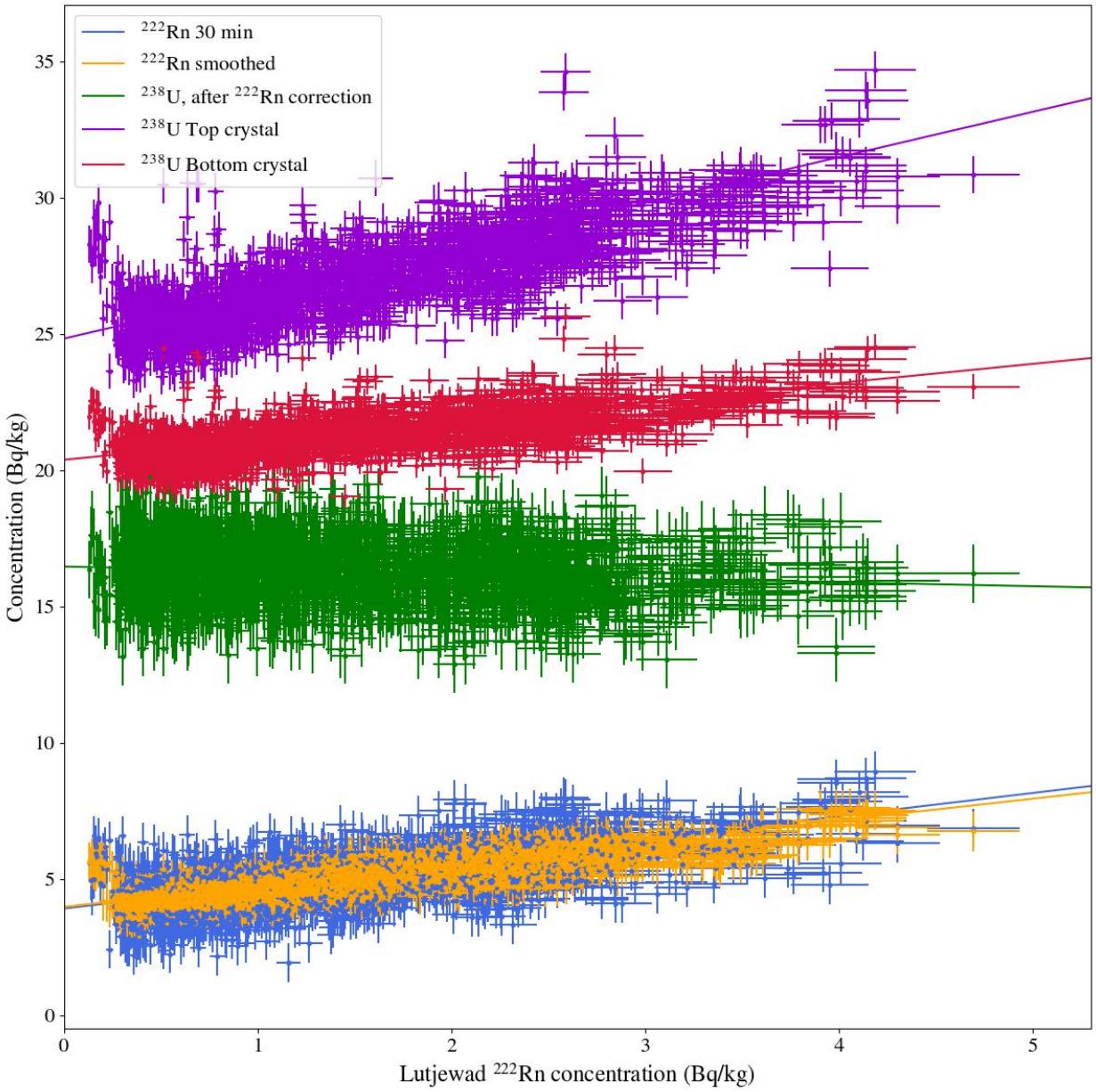

Figure 6.8: The concentrations of ^{238}U and ^{222}Rn measured by the split detector vs the atmospheric ^{222}Rn concentration measured by Lutjewad.

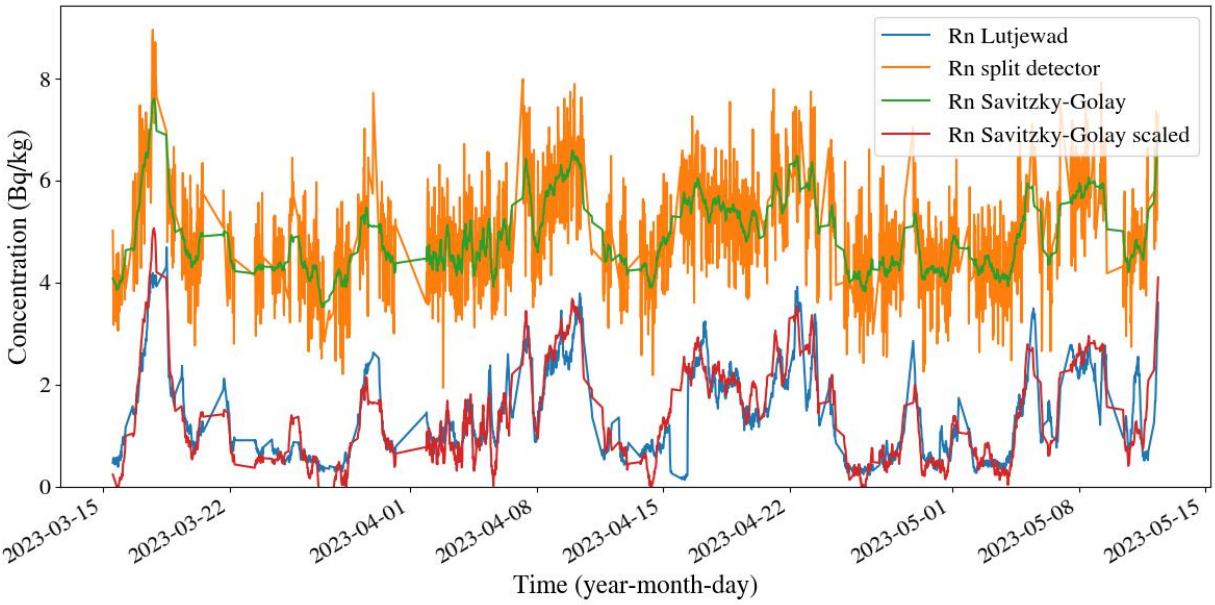

Figure 6.9: The timeline of the ^{222}Rn concentration in Bq/kg as measured by Lutjewad and the split detector with crystal 1 facing up. The green line was obtained by applying a Savitzky-Golay filter of window size 19 and polynomial order 1. The red line is the same as the green, but shifted and scaled by finding the inverse of the linear fit of Figure 6.8 for the smoothed data $y = 0.73x + 3.91$.

coefficient is increased from $r = 0.64$ to $r = 0.88$. The resulting Savitzky-Golay filtered ^{222}Rn concentration is illustrated over time in Figure 6.9. These parameters were optimised specifically for this dataset, these exact parameters may therefore not be optimal for other data sets. The split detector ^{222}Rn measurement can be transformed to better match the Lutjewad ^{222}Rn measurement using the linear fit shown in Figure 6.8, with the slope and intercept found for ^{222}Rn Smoothed in Table 6.1.

6.4.1 Flipping the detector

During the measurement using the split detector, it was observed that the concentrations of the radionuclides were not equal in both crystals. For ^{238}U that is in part due to radon, but not for the other radionuclides. The top crystal measured about 5 % less ^{40}K, and 41 % more ^{137}Cs than the bottom crystal. The difference in ^{232}Th was only about 1 %. This is shown in Table 6.2. Additionally, the radon concentration measured by the split detector was consistently higher than the radon concentration measured by Lutjewad. Consequently, in order to proceed with the measurements, the detector was inverted, with crystal 2 now facing upwards. The detector underwent flipping on May 12th, and only the data collected until 2 pm on May 26th is considered for this analysis. It is noteworthy that the ^{222}Rn data from Lutjewad is available until May 21st.

of data with values of $n = 1$ and $m = 19$

Nuclide	Crystal 1 top	Crystal 2 bottom	Crystal 2 top	Crystal 1 bottom
^{40}K	251.57 ± 0.07	265.85 ± 0.06	260.9 ± 0.2	279.6 ± 0.2
^{238}U*	28.82 ± 0.01	22.38 ± 0.01	26.67 ± 0.02	22.33 ± 0.02
^{232}Th	26.98 ± 0.01	26.69 ± 0.01	27.87 ± 0.02	26.88 ± 0.01
^{137}Cs	5.08 ± 0.01	3.59 ± 0.01	5.04 ± 0.02	3.93 ± 0.01

Table 6.2: The radionuclide concentrations in Bq/kg, measured by the crystal 1 and crystal 2 in both orientations. This was calculated from the spectra of the entire measurement. *Note that ^{238}U has differences between top and bottom, in part due to the presence of ^{222}Rn.

After the detector was flipped, the mean concentrations it measured in each crystal changed by less than 5 %. The top crystal again measured more ^{238}U, ^{137}Cs and ^{232}Th and the bottom again measured more ^{40}K. The corrected uranium concentration in this measurement was 18 ± 2 Bq/kg. The correlation of the both measurements are shown in Figure 6.10, and the parameters of linear fit and correlation coefficients are given in Table 6.3.

	Slope	Intercept	r
^{222}Rn	0.83	2.86	0.72
^{222}Rn Smoothed	0.81	2.89	0.93
^{228}U Corrected	-0.09	18.3	-0.08
^{228}U Top	1.69	24.4	0.84
^{228}U Bottom	0.74	21.2	0.73

Table 6.3: The parameters of the linear fit of the data shown in Figure 6.10

Similar as for crystal 1 facing up, the concentrations of ^{238}U in the top and bottom crystals correlate positively with the radon concentration. After ^{222}Rn correction, the ^{238}U concentration is weakly negatively correlated to the ^{222}Rn concentration. With crystal 2 pointed up, the split detector consistently measures a higher concentration of ^{222}Rn than Lutjewad. The intercept of the linear fit is smaller with it being $r = 2.89$ instead of $r = 3.85$. The two concentrations correlate positively in this orientation as well, with a correlation coefficient of $r = 0.72$, and the correlation can again be improved (to $r = 0.93$), by applying a Savitzky-Golay filter.

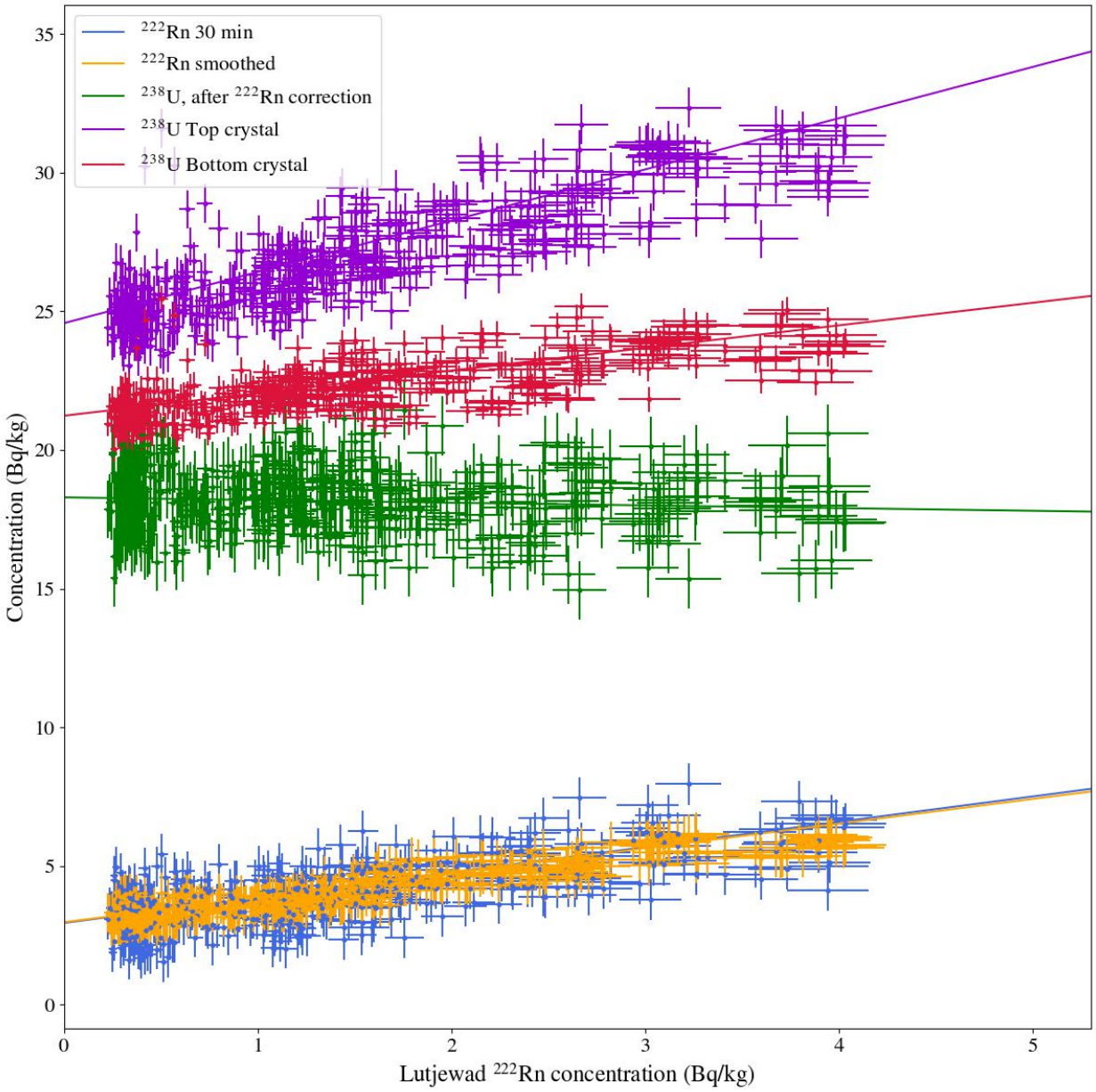

Figure 6.10: The concentrations of ^{238}U and ^{222}Rn measured by the split detector with crystal 2 facing up vs the atmospheric ^{222}Rn concentration measured by Lutjewad.

The raw and Savitzky-Golay filtered data of the split detector ^{222}Rn data are shown alongside the Lutjewad radon data in Figure 6.11. The split detector clearly measures a higher ^{222}Rn concentration than Lutjewad throughout the whole upside down measurement. The split detector ^{222}Rn measurement can be transformed to better match the Lutjewad ^{222}Rn measurement using the linear fit shown in Figure 6.10, with the slope and intercept found for ^{222}Rn Smoothed in Table 6.3.

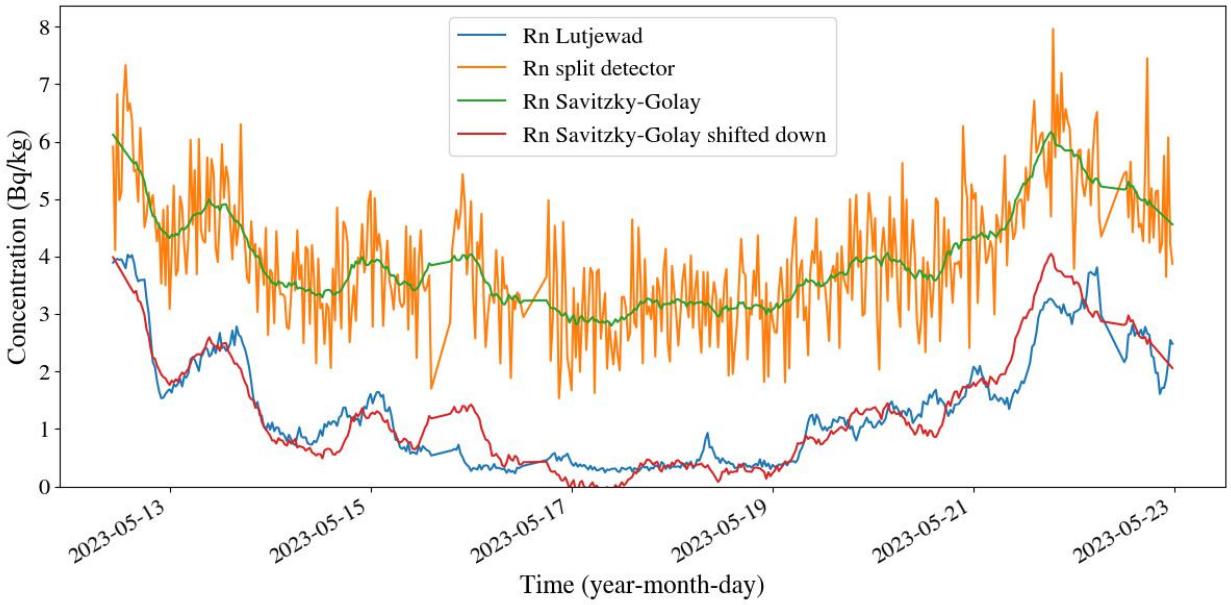

Figure 6.11: The timeline of the ^{222}Rn concentration in Bq/kg as measured by Lutjewad and the split detector with crystal 2 facing up. The green line was obtained by applying a Savitzky-Golay filter of window size 19 and polynomial order 1. The red line is the same as the green, but shifted and scaled by finding the inverse of the linear fit of Figure 6.10 for the smoothed data $y = 0.81x + 2.89$.

6.5 Discussion and conclusions

The split detector is designed as a measurement tool to compensate for the presence of ^{222}Rn during geophysical surveys. In order to evaluate its effectiveness, the split detector was employed for a stationary measurement at Lutjewad, an atmospheric measurement station. In this context, the response of the detectors could be correlated with the atmospheric concentrations of ^{222}Rn that were measured at Lutjewad.

During rain, the split detector proves to be ineffective in terms of correcting for ^{222}Rn or determining ^{238}U concentrations in the soil. Significant spikes in ^{238}U radiation are observed during this period, attributable to radioactive aerosols that settle with the rainfall. Peaks in concentration are already measured at less than 0.5 mm/h of rain. As a consequence, the measured concentrations of atmospheric ^{222}Rn and ^{238}U in the soil become distorted. This result substantiates the work done in 2011 by Bottardi et al. [19].

6.5.1 Split detector as a ^{222}Rn correction method

During the measurement process, there is a positive correlation between the ^{238}U concentrations in the upper and lower crystals and the atmospheric ^{222}Rn concentration. This correlation confirms that ^{222}Rn acts as a background factor in geophysical γ-ray

surveys. After applying the ^{222}Rn correction method (equation 3.4), we obtained a ^{238}U concentration that exhibits a small negative correlation with crystal 1 ($r = -0.1$) or crystal 2 ($r = -0.08$) looking up with respect to the atmospheric ^{222}Rn concentration. The coefficient of determination, R^2, measures the proportion of the variance in the ^{238}U concentration that can be explained by the variance in the ^{238}U concentration measured by Lutjewad. In the measurement with crystal 1 up, this means, $R^2 = 0.01$, indicating that only 1% of the variance in the ^{238}U concentration can be explained by the variance in the Lutjewad measurements. **Therefore, the split detector ^{222}Rn correction method successfully removes the influence of ^{222}Rn on the measured ^{238}U concentration in geophysical surveys.**

While the split detector was able to successfully reduce the ^{222}Rn dependence in the measurement of the ^{238}U concentration, the intercepts of the linear regressions for the ^{238}U concentrations in the upper and lower crystal regions did not align. Assuming Lutjewad measures the true value of ^{222}Rn, this suggests that there is some inaccuracy in the theoretical model, or calibration of the device. Naively applying the correction method, different intercepts lead to an adjusted ^{238}U concentration, even without ^{222}Rn presence.

Flipping the detector already changed the parameters of the linear fits, this indicates that the detector is sensitive to changes. More research can be done to look to optimize calibration parameters more in order to find more accurate absolute values of the ^{238}U concentration. For this, a different method of measuring the ^{238}U concentration can be done around Lutjewad can be done to check the accuracy of the measurement that was done first.

Inaccuracies in the theoretical model could include the differences in geometry between simulation and reality. This can be checked by designing a simulation which is more similar to the measurement situation (include the Wadden Sea dyke and scaffold) and analysing the data using that simulation. The ^{232}Th, ^{137}Cs and ^{40}K concentrations should ideally be the same in both crystals. In the orientation with crystal 1 on top, ^{232}Th was almost the same in both crystals, otherwise this was not the case. A difference in simulation and reality could also be responsible for these changes. With ^{137}Cs, the difference might be due to how low the concentrations present at Lutjewad are. Removing ^{137}Cs from the analysis may change the concentrations of the other radionuclides, and should thus be attempted to see how the results change.

6.5.2 The split detector as a ^{222}Rn measurement system

The measurements of ^{222}Rn obtained from the split detector exhibit a correlation with the measurements from Lutjewad, with correlation coefficients of $r = 0.64$ with crystal 1 on top and $r = 0.72$ with crystal 2 on top; however, they do not yield identical results. Additionally, the data obtained in 30-minute intervals has noise due to the statistical uncertainty of measurements. By applying a Savitzky-Golay filter, the ^{222}Rn signal is

smoothed, resulting in an improvement in the correlation between the ^{222}Rn measurements from both sources. The correlation coefficients are improved to $r = 0.88$ with crystal 1 on top and $r = 0.93$ with crystal 2 on top. However, in this particular case, the Savitzky-Golay filter was applied to points with a time interval of 30 minutes between them. The optimal correlation was achieved by smoothing over a time period of 9 hours and 30 minutes. Which is much longer than a typical geophysical survey, especially with a drone. To use the split detector as a ^{222}Rn measurement device, it is best used for periods of time that allow Savitzky-Golay filters with a window size m of several hours to be applied.

A linear regression analysis performed on the ^{222}Rn measurements of both the split detector and Lutjewad reveals a non-zero intercept. Assuming Lutjewad measures the true value of ^{222}Rn, this suggests that there is some inaccuracy in the theoretical model, or calibration of the device. A solution in this scenario was to use the linear regression slope and intercept to transform the split detector ^{222}Rn data such that it matches that of Lutjewad. This solution is essentially an extra calibration step for the situation where you would want to use the split detector as an atmospheric ^{222}Rn monitoring device. The linear fit correction to the ^{222}Rn measurement is specific to a measurement geometry, detector orientation, and can not generally be applied for ^{222}Rn measurements.

The deviation in the measured ^{222}Rn concentration between the split detector and Lutjewad could stem from either a disparity between the theoretical model used in simulations and the actual measurement conditions, or a calibration issue with the detector itself. To investigate the calibration problem, an experiment was conducted by flipping the detector upside down. This test resulted in slightly different values for each radionuclide, but it did not eliminate the disparity in measured ^{222}Rn concentrations. The discrepancy in measured ^{222}Rn concentrations between the split detector and Lutjewad, can in part be attributed to a difference between the theoretical model and the real-life conditions. Further research is required to better understand why Lutjewad and the split detector measure a different concentration of ^{222}Rn, including simulations which include more features of the measurement geometry and perhaps non-homogeneous ^{222}Rn concentrations.

The split detector can be used as an atmospheric ^{222}Rn detector, however more research is required to make sure it can be calibrated to determine the correct amounts of ^{222}Rn.

Chapter 7

Discussion and Conclusion

This thesis encompasses a research project conducted at Medusa Radiometrics, a company specializing in the development and production of γ-ray spectrometers and accompanying analysis software. Their γ-ray spectrometers are specifically designed for application in geophysical surveys. Geophysical γ-ray surveys aim to assess the concentrations of various radionuclides present in the soil, with a primary focus on ^{40}K, ^{232}Th, and ^{238}U. By acquiring knowledge of radionuclide concentrations in the soil, γ-ray spectrometers indirectly provide valuable insights into other soil properties.

One of the radionuclides in this context is ^{222}Rn, a noble gas that is generated as part of the decay chain of ^{238}U and is naturally present in the ground. After its production, ^{222}Rn has the ability to escape from the soil into the atmosphere, where it subsequently undergoes radioactive decay. The challenge arises because the γ-ray spectrum emitted by ^{222}Rn is similar to that of ^{238}U. Consequently, this can lead to measured ^{238}U concentrations in the soil that appear higher than their actual values.

Multiple techniques have been developed to address the issue of ^{222}Rn presence, with most of them originally designed for airborne γ-ray surveys. In the research conducted by S. van der Veeke [11], two novel ^{222}Rn correction methods were introduced specifically for UAV-based geophysical γ-ray surveys. One of these approaches involved the utilization of a split γ-ray spectrometer, which consists of two scintillation crystals: one positioned upwards and the other downwards. This detector exhibits directional sensitivity, enabling it to differentiate between ^{238}U-related radiation originating from the ground (associated with ^{238}U) and radiation stemming from the air (linked to ^{222}Rn). To validate the concept, a prototype of this split detector was constructed by Medusa Radiometrics.

7.1 Calibration

The split detector underwent a calibration process involving several steps. Initially, Monte Carlo simulations were employed to determine the theoretical response of the split detector within the calibration setup at Medusa Radiometrics, known as Stonehenge. This theoretical response was subsequently compared to the actual measurement obtained using the split detector in the Stonehenge calibration setup. This comparison facilitated the determination of calibration parameters. With the calibration parameters established, the detector can be utilized in simulations of various geometries, enabling its application in geophysical surveys.

The split detector's directional sensitivity allowed for the assessment of radiation isotropy at Stonehenge, revealing that it was not evenly distributed in all directions. The simulations indicated 0.7 ± 0.1 % (0.4 ± 0.1% for ^{40}K) higher radiation intensity originating from above, whereas the measurements indicated a higher intensity of radiation coming from below. For crystal 1 and crystal 2 respectively, 1.6 ± 0.1 % and 0.7 ± 0.1 % higher intensity was measured when facing down.

Additional investigations of the Stonehenge calibration setup can be conducted to explore its horizontal asymmetry. This can be accomplished by conducting measurements and simulations within the setup while orienting the detector in such a way that each crystal faces a horizontal direction. If it is discovered that Stonehenge is more symmetric horizontally in both simulation and reality, this approach would provide a more accurate calibration method with reduced disparities between simulation and real-world measurements.

7.2 Rotations

The directional sensitivity of the split detector can introduce errors in the estimation of radionuclide concentrations if it is not positioned correctly during a survey. To investigate the rotational dependence of the split detector, both simulations and measurements were conducted. A geometric hypothesis was formulated suggesting that the relative radiation intensity measured by each crystal could be approximated by a cosine function. The geometric hypothesis was shown to be a good approximation in both measurement and simulation. The simulations revealed a slight deviation of 0.5 percentage points from this expected behaviour for rotations around the detector's z-axis for atmospheric ^{222}Rn (refer to Figure 5.1).

The geometric hypothesis is close enough that it can be applied as a correction method in field measurements. This however should still be tested by measuring at multiple angles and applying corrections based up equation 5.1. It can also be tested in the context of a geophysical survey with a UAV, which collects angular data during the flight. Uncorrected

and corrected measurements can be compared to see if corrections are necessary during geophysical surveys.

7.3 Radon measurement

The detector was deployed for a stationary measurement at the Lutjewad atmospheric measurement station. Here, the measurements of the split detector could be correlated with ^{222}Rn measurements done at Lutjewad.

Based on the findings, it is advised not to utilize the split detector during rain. This is because the radioactive daughters of ^{222}Rn, which are attached to aerosols, tend to settle on the ground during rainfall. Consequently, if the detector is used in such conditions, it will register elevated concentrations of ^{238}U.

The investigation revealed that after implementing the ^{222}Rn correction for the ^{238}U concentration, there is minimal to no correlation of the measured ^{238}U in the ground with the atmospheric ^{222}Rn concentration. This indicates that the split detector method effectively eliminates the ^{222}Rn background during geophysical measurements.

It was observed that the ^{222}Rn concentration measured by the split detector is higher than that measured by Lutjewad. This is related to the fact that with the used model, the linear fit predicts that a different ^{238}U concentration would be measured by both crystals even in absence of ^{222}Rn. This leads to the hypothesis that the measured ^{238}U concentration is underestimated and a ^{222}Rn concentration is overestimated. This can be tested by doing an independent measurement of the ^{238}U concentration in the ground at Lutjewad, which would confirm if the ^{238}U concentration is underestimated.

The ^{222}Rn concentration measured by the split detector does exhibit correlation with the measurements obtained by Lutjewad. However, the data collected by the split detector is characterized by a significant amount of noise. To enhance the correlation between the two ^{222}Rn measurements, a Savitzky-Golay filter can be applied. It is important to note that this filtering method performs better with a larger dataset. Therefore, a longer measurement time is preferable when utilizing the split detector as a ^{222}Rn detector. Long measurements are not practical or necessary in the context of geophysical surveys, where the goal is to measure the radionuclide concentrations in the ground rather than in the air. If the goal is to use the split detector for the purpose of atmospheric ^{222}Rn monitoring, the Savitzky-Golay filter is a useful tool to smoothen out the acquired data.

Further research is necessary to validate its accuracy in measuring both ^{222}Rn and ^{238}U concentrations, as well a ^{40}K, ^{232}Th and ^{137}Cs. This includes analysis of the data acquired at Lutjewad without the inclusion of ^{137}Cs and/or with simulations that more closely match the measurement geometry. Additionally, the split detector is yet to be used during

a geophysical survey. Performing a geophysical survey with the split detector, will come with additional challenges, such as matching the radionuclide concentrations measured by the top and bottom crystal. Refinement of calibration parameters can be done to improve the reliability and precision of the measurements obtained using the split detector.

To conclude, the split detector demonstrates promise as an effective tool for mitigating the influence of ^{222}Rn signals in geophysical surveys.

Acknowledgements

I would like to conclude this thesis by expressing my gratitude to the individuals who have contributed to the completion of this research.

I would like to express my sincere gratitude to the individuals at Medusa Radiometrics, whose invaluable contributions made this research possible. A special thanks goes to Steven van der Veeke, whose PhD thesis served as the foundation and inspiration for this study. His support and guidance were instrumental in the successful completion of this research project. I am also grateful to Lennart Blaauw for introducing me to MCNP and for his assistance in calibrating the split detector. Additionally, I would like to acknowledge Samantha van der Veen for her contributions in constructing the split detector. Throughout the project, Han Limburg and Marco Tijs provided valuable assistance and support, for which I am truly thankful. I would also like to extend my appreciation to the entire team at Medusa Radiometrics, Medusa Explorations, EVABits, and de Wegenscanners for fostering a pleasant and conducive work environment during my time at Medusa Radiometrics.

I would like to express my appreciation to the individuals from CIO/Lutjewad who played a crucial role in enabling the experiment conducted at their facility. I am grateful to Bert Kers, who generously provided guidance and assistance in navigating the premises and installing the measurement setup. A special thanks goes to Bert Scheeren for his responsibility in supplying the Radon data from Lutjewad, which was essential for the success of this research endeavor. I would also like to thank Ramon Richie for his invaluable support in establishing a remote connection to the split detector, making it feasible to carry out the experiment effectively. Thanks also to Harro Meijer who played an important role in enabling the collaboration with CIO. Their contributions were instrumental in facilitating the smooth execution of the project, and I am grateful for their assistance and collaboration.
Lastly, I would like to extend my sincere gratitude to Dr. Emiel van der Graaf for introducing me to this project and for his insightful feedback on my writing.

Bibliography

[1] Medusa Radiometrics. "Medusa website." (2023), [Online]. Available: https://medusa-online.com/en/ (visited on 06/05/2023).

[2] *Guidelines for Radioelement Mapping Using Gamma Ray Spectrometry Data* (TECDOC Series 1363). Vienna: INTERNATIONAL ATOMIC ENERGY AGENCY, 2003, ISBN: 92-0-108303-3. [Online]. Available: https://www.iaea.org/publications/6746/guidelines-for-radioelement-mapping-using-gamma-ray-spectrometry-data.

[3] R. Koomans, S. de Vries, and J. Limburg, "An underwater gamma spectrometer as tool for ecological assessment," in *Near Surface Geoscience 2016-Second Applied Shallow Marine Geophysics Conference*, EAGE Publications BV, vol. 2016, 2016, pp. 1–5.

[4] R. Koomans and R. De Meijer, "Density gradation in cross-shore sediment transport," *Coastal engineering*, vol. 51, no. 11-12, pp. 1105–1115, 2004.

[5] M. Van Wijngaarden, L. Venema, R. De Meijer, J. Zwolsman, B. Van Os, and J. Gieske, "Radiometric sand–mud characterisation in the rhine–meuse estuary: Part a. fingerprinting," *Geomorphology*, vol. 43, no. 1-2, pp. 87–101, 2002.

[6] R. Koomans, V. der Veeke, P. Jacobs, and H. Limburg, "Mapping sediment contamination with a gamma-ray spectrometer, underwater and on land," in *25th European Meeting of Environmental and Engineering Geophysics*, EAGE Publications BV, vol. 2019, 2019, pp. 1–5.

[7] E. Van der Graaf, R. Koomans, J. Limburg, and K. De Vries, "In situ radiometric mapping as a proxy of sediment contamination: Assessment of the underlying geochemical and-physical principles," *Applied radiation and isotopes*, vol. 65, no. 5, pp. 619–633, 2007.

[8] S. Pätzold, M. Leenen, and T. W. Heggemann, "Proximal mobile gamma spectrometry as tool for precision farming and field experimentation," *Soil Systems*, vol. 4, no. 2, p. 31, 2020.

[9] E. Van der Klooster, F. Van Egmond, and M. Sonneveld, "Mapping soil clay contents in dutch marine districts using gamma-ray spectrometry," *European Journal of Soil Science*, vol. 62, no. 5, pp. 743–753, 2011.

[10] *Airborne gamma ray spectrometer surveying.* (technical reports series 323). Vienna: INTERNATIONAL ATOMIC ENERGY AGENCY, 1991. [Online]. Available: https://inis.iaea.org/collection/NCLCollectionStore/_Public/22/072/22072114.pdf.

[11] S. van der Veeke, *UAV-borne radioelement mapping: Towards a guideline and Verification Methods for geophysical field measurements.* University of Groningen, 2023.

[12] IAEA. "Live chart of nuclides." (2022), [Online]. Available: https://www-nds.iaea.org/relnsd/vcharthtml/VChartHTML.html#dcy2 (visited on 02/17/2023).

[13] F. Kondev, M. Wang, W. Huang, S. Naimi, and G. Audi, "The nubase2020 evaluation of nuclear physics properties *," *Chinese Physics C*, vol. 45, no. 3, p. 030 001, Mar. 2021. DOI: 10.1088/1674-1137/abddae. [Online]. Available: https://dx.doi.org/10.1088/1674-1137/abddae.

[14] G. F. Knoll, "Radiation Detection and Measurement, 3rd ed.," in 3rd edition. New York: John Wiley and Sons, 2000, ch. 2, ISBN: 978-0-471-07338-3, 978-0-471-07338-3.

[15] J. E. Turner, "Interaction of photons with matter," in *Atoms, Radiation, and Radiation Protection.* John Wiley & Sons, Ltd, 2007, ch. 8, pp. 173–208, ISBN: 9783527616978. DOI: https://doi.org/10.1002/9783527616978.ch8.

[16] P. Hendriks, J. Limburg, and R. de Meijer, "Full-spectrum analysis of natural γ-ray spectra," *Journal of Environmental Radioactivity*, vol. 53, no. 3, pp. 365–380, 2001, Environmental Radiometrics, ISSN: 0265-931X. DOI: https://doi.org/10.1016/S0265-931X(00)00142-9. [Online]. Available: https://www.sciencedirect.com/science/article/pii/S0265931X00001429.

[17] M. R. James, D. B. Pelowitz, A. J. Fallgren, *et al.*, "MCNP6™ User's Manual Code Version 6.1.1 Beta," Los Alamos National Laboratory, Los Alamos, NM, USA, Tech. Rep. LA-CP-14-00745, Jun. 2014, This document is provided in the MCNP6 release package available from RSICC and is not accessible from the MCNP website.

[18] J. A. Kulesza, T. R. Adams, J. C. Armstrong, *et al.*, "MCNP® Code Version 6.3.0 Theory & User Manual," Los Alamos National Laboratory, Los Alamos, NM, USA, Tech. Rep. LA-UR-22-30006, Rev. 1, Sep. 2022. DOI: 10.2172/1889957. [Online]. Available: https://www.osti.gov/biblio/1889957.

[19] C. Bottardi, M. Albéri, M. Baldoncini, *et al.*, "Rain rate and radon daughters' activity," *Atmospheric Environment*, vol. 238, p. 117 728, 2020, ISSN: 1352-2310. DOI: https://doi.org/10.1016/j.atmosenv.2020.117728. [Online]. Available: https://www.sciencedirect.com/science/article/pii/S135223102030460X.

[20] J. H. Hubbell and S. M. Seltzer. "X-ray mass attenuation coefficients." (2004), [Online]. Available: https://physics.nist.gov/PhysRefData/XrayMassCoef/ComTab/air.html (visited on 03/28/2023).

[21] A. G. Williams, S. D. Chambers, F. Conen, *et al.*, "Radon as a tracer of atmospheric influences on traffic-related air pollution in a small inland city," *Tellus B: Chemical and Physical Meteorology*, vol. 68, no. 1, p. 30 967, 2016.

[22] A. Röttger, S. Röttger, C. Grossi, *et al.*, "New metrology for radon at the environmental level," *Measurement Science and Technology*, vol. 32, no. 12, p. 124 008, 2021.

[23] A. C. George, "World history of radon research and measurement from the early 1900's to today," *AIP Conference Proceedings*, vol. 1034, no. 1, pp. 20–33, 2008. DOI: 10.1063/1.2991210. eprint: https://aip.scitation.org/doi/pdf/10.1063/1.2991210. [Online]. Available: https://aip.scitation.org/doi/abs/10.1063/1.2991210.

[24] Centrum voor IsotopenOnderzoek (CIO), ESRIG, University of Groningen, Groningen, the Netherlands, "Lutjewad radon data 2006- jan 2023," 2023.

[25] S. Oikawa, N. Kanno, T. Sanada, *et al.*, "A nationwide survey of outdoor radon concentration in japan," *Journal of Environmental Radioactivity*, vol. 65, no. 2, pp. 203–213, 2003, ISSN: 0265-931X. DOI: https://doi.org/10.1016/S0265-931X(02)00097-8. [Online]. Available: https://www.sciencedirect.com/science/article/pii/S0265931X02000978.

[26] J. Porstendörfer, "Properties and behaviour of radon and thoron and their decay products in the air," *Journal of Aerosol Science*, vol. 25, no. 2, pp. 219–263, 1994, ISSN: 0021-8502. DOI: https://doi.org/10.1016/0021-8502(94)90077-9. [Online]. Available: https://www.sciencedirect.com/science/article/pii/0021850294900779.

[27] A. Podstawczyńska, K. Kozak, W. Pawlak, and J. Mazur, "Seasonal and diurnal variation of outdoor radon (222rn) concentrations in urban and rural area with reference to meteorological conditions," *Nukleonika*, vol. 55, no. 4, pp. 543–547, 2010.

[28] D. Tchorz-Trzeciakiewicz and M. Kłos, "Factors affecting atmospheric radon concentration, human health," *Science of the total environment*, vol. 584, pp. 911–920, 2017.

[29] A. Vargas, D. Arnold, J. Adame, C. Grossi, M. Hernández-Ceballos, and J. Bolivar, "Analysis of the vertical radon structure at the spanish "el arenosillo" tower station," *Journal of Environmental Radioactivity*, vol. 139, pp. 1–17, 2015, ISSN: 0265-931X. DOI: https://doi.org/10.1016/j.jenvrad.2014.09.018. [Online]. Available: https://www.sciencedirect.com/science/article/pii/S0265931X14002847.

[30] J. Porstendörfer, G. Butterweck, and A. Reineking, "Diurnal variation of the concentrations of radon and its short-lived daughters in the atmosphere near the ground," *Atmospheric Environment. Part A. General Topics*, vol. 25, no. 3, pp. 709–713, 1991, ISSN: 0960-1686. DOI: https://doi.org/10.1016/0960-1686(91)90069-J. [Online]. Available: https://www.sciencedirect.com/science/article/pii/096016869190069J.

[31] S. De Francesco, F. P. Tommasone, E. Cuoco, G. Verrengia, and D. Tedesco, "Radon hazard in shallow groundwaters: Amplification and long term variability induced by rainfall," *Science of the total environment*, vol. 408, no. 4, pp. 779–789, 2010.

[32] H. Hötzl and R. Winkler, "Long-term variation of outdoor radon equilibrium equivalent concentration," *Radiation and environmental biophysics*, vol. 33, no. 4, pp. 381–392, 1994.

[33] L. L. Lloyd and M. O'Connell, "Evaluation of radon sources and phosphate slag in butte, montana," Montana Dept. of Health and Environmental Sciences, Helena (USA), Tech. Rep., 1983.

[34] D. J. Steck, R. W. Field, and C. F. Lynch, "Exposure to atmospheric radon.," *Environmental Health Perspectives*, vol. 107, no. 2, pp. 123–127, 1999.

[35] J. H. Seinfeld, "Es&t books: Atmospheric chemistry and physics of air pollution," *Environmental science & technology*, vol. 20, no. 9, pp. 863–863, 1986.

[36] C. Y. Chao, T. C. Tung, and J. Burnett, "Influence of ventilation on indoor radon level," *Building and Environment*, vol. 32, no. 6, pp. 527–534, 1997, ISSN: 0360-1323. DOI: https://doi.org/10.1016/S0360-1323(97)00017-6. [Online]. Available: https://www.sciencedirect.com/science/article/pii/S0360132397000176.

[37] M. Magalhães, E. Amaral, I. Sachett, and E. Rochedo, "Radon-222 in brazil: An outline of indoor and outdoor measurements," *Journal of Environmental Radioactivity*, vol. 67, no. 2, pp. 131–143, 2003, ISSN: 0265-931X. DOI: https://doi.org/10.1016/S0265-931X(02)00175-3. [Online]. Available: https://www.sciencedirect.com/science/article/pii/S0265931X02001753.

[38] R. De Meijer, L. Put, R. Bergman, *et al.*, "Local variations of outdoor radon concentrations in the netherlands and physical properties of sand with enhanced natural radioactivity," *Science of the Total Environment*, vol. 45, pp. 101–109, 1985.

[39] N. Eresmaa, A. Karppinen, S. Joffre, J. Räsänen, and H. Talvitie, "Mixing height determination by ceilometer," *Atmospheric Chemistry and Physics*, vol. 6, no. 6, pp. 1485–1493, 2006.

[40] KNMI. "Determination of the mixing layer height from ceilometer backscatter profiles." (2007), [Online]. Available: https://www.knmi.nl/kennis-en-datacentrum/achtergrond/determination-of-the-mixing-layer-height-from-ceilometer-backscatter-profiles (visited on 04/12/2023).

[41] M. Davies, "Chapter 12 - air quality modeling in the athabasca oil sands region," in *Alberta Oil Sands*, ser. Developments in Environmental Science, K. E. Percy, Ed., vol. 11, Elsevier, 2012, pp. 267–309. DOI: https://doi.org/10.1016/B978-0-08-097760-7.00012-3. [Online]. Available: https://www.sciencedirect.com/science/article/pii/B9780080977607000123.

[42] M. Baldoncini, M. Albéri, C. Bottardi, *et al.*, "Exploring atmospheric radon with airborne gamma-ray spectroscopy," *Atmospheric Environment*, vol. 170, pp. 259–268, 2017, ISSN: 1352-2310. DOI: https://doi.org/10.1016/j.atmosenv.2017.09.048. [Online]. Available: https://www.sciencedirect.com/science/article/pii/S1352231017306477.

[43] B. R. Minty, "Multichannel models for the estimation of radon background in airborne gamma-ray spectrometry," *Geophysics*, vol. 63, no. 6, pp. 1986–1996, 1998.

[44] P. Killeen, C. Mwenifumbo, and K. Ford, "11.14 - tools and techniques: Radiometric methods," in *Treatise on Geophysics (Second Edition)*, G. Schubert, Ed., Second Edition, Oxford: Elsevier, 2015, pp. 447–524, ISBN: 978-0-444-53803-1. DOI: https://doi.org/10.1016/B978-0-444-53802-4.00209-8. [Online]. Available: https://www.sciencedirect.com/science/article/pii/B9780444538024002098.

[45] B. R. Minty, "Airborne gamma-ray spectrometric background estimation using full spectrum analysis," *Geophysics*, vol. 57, no. 2, pp. 279–287, 1992.

[46] R. Grasty and J. Hovgaard, "The calibration of upward looking detectors in gamma ray surveys.," in *SEG Technical Program Expanded Abstracts 1996*, Society of Exploration Geophysicists, 1996, pp. 1422–1425.

[47] P. Jurza, I. Campbell, P. Robinson, R. Wackerle, P. Cunneen, and B. Pavlík, "Use of 214pb photopeaks for radon removal: Utilising current airborne gamma-ray spectrometer technology and data processing," *Exploration Geophysics*, vol. 36, no. 3, pp. 322–328, 2005.

[48] J. Xia, B. Song, Y. Gu, *et al.*, "Application of advanced spectral-ratio radon background correction in the uav-borne gamma-ray spectrometry," *Nuclear Engineering and Technology*, 2023, ISSN: 1738-5733. DOI: https://doi.org/10.1016/j.net.2023.04.034. [Online]. Available: https://www.sciencedirect.com/science/article/pii/S1738573323002127.

[49] B. Minty and P. McFadden, "Improved nasvd smoothing of airborne gamma–ray spectra," *Exploration Geophysics*, vol. 29, no. 3-4, pp. 516–523, 1998.

[50] E. Van der Graaf, J. Limburg, R. Koomans, and M. Tijs, "Monte carlo based calibration of scintillation detectors for laboratory and in situ gamma ray measurements," *Journal of environmental radioactivity*, vol. 102, no. 3, pp. 270–282, 2011.

[51] M. Abramowitz, *Handbook of Mathematical Functions, With Formulas, Graphs, and Mathematical Tables,* USA: Dover Publications, Inc., 1974, ISBN: 0486612724.

[52] Medusa. "The products of medusa." (2023), [Online]. Available: https://medusa-online.com/en/products/sensors/ (visited on 05/06/2023).

[53] Medusa. "Calibration of spectral gamma tools." (2023), [Online]. Available: https://the.medusa.institute/wiki/calibration-of-spectral-gamma-tools (visited on 05/11/2023).

[54] Medusa. "Medusa calibration procedure." (2023), [Online]. Available: https://docs.medusa-radiometrics.com/technical-info/Working-version/calibration-procedure# (visited on 05/11/2023).

[55] Y.-H. Tu, S. Phinn, K. Johansen, A. Robson, and D. Wu, "Optimising drone flight planning for measuring horticultural tree crop structure," *ISPRS Journal of Photogrammetry and Remote Sensing*, vol. 160, pp. 83–96, 2020.

[56] M. Aljehani, M. Inoue, A. Watanbe, T. Yokemura, F. Ogyu, and H. Iida, "Uav communication system integrated into network traversal with mobility," *SN Applied Sciences*, vol. 2, pp. 1–20, 2020.

[57] R. Groningen. "Lutjewad measurement station." (2023), [Online]. Available: https://www.rug.nl/research/centre-for-isotope-research/research/atmospheric-measurement-stations/lutjewad/ (visited on 05/30/2023).

[58] R. observatory. "Lutjewad." (2023), [Online]. Available: https://ruisdael-observatory.nl/lutjewad/ (visited on 05/30/2023).

[59] S. Whittlestone and W. Zahorowski, "Baseline radon detectors for shipboard use: Development and deployment in the first aerosol characterization experiment (ace 1)," *Journal of Geophysical Research: Atmospheres*, vol. 103, no. D13, pp. 16 743–16 751, 1998.

[60] V. D. Laan, U. Karstens, R. Neubert, V. D. Laan-Luijkx, and H. Meijer, "Observation-based estimates of fossil fuel-derived co2 emissions in the netherlands using Δ14c, co and 222radon," *Tellus B: Chemical and Physical Meteorology*, vol. 62, no. 5, pp. 389–402, 2010.

[61] Aerodata International Surveys, CNES / Airbus, GeoContent, Maxar Technologies, and Google. "Google maps image of lutjewad." (2023), [Online]. Available: https://www.google.com/maps/@53.4038185,6.351574,304m/data=!3m1!1e3?entry=ttu (visited on 06/01/2023).

[62] KNMI. "Uurgegevens lauwersoog." (2023), [Online]. Available: https://www.knmi.nl/nederland-nu/klimatologie/uurgegevens (visited on 05/26/2023).

[63] A. Savitzky and M. J. Golay, "Smoothing and differentiation of data by simplified least squares procedures.," *Analytical chemistry*, vol. 36, no. 8, pp. 1627–1639, 1964.